AFRL-RY-WP-TR-2022-0269

DENSELY PACKED 2D PHOTONIC PHASED ARRAY USING SEMICONDUCTOR MONOLAYERS

Ipshita Datta and Michal Lipson
Columbia University

NOVEMBER 2022
Final Report

STINFO COPY

AIR FORCE RESEARCH LABORATORY
SENSORS DIRECTORATE
WRIGHT-PATTERSON AIR FORCE BASE, OH 45433-7320
AIR FORCE MATERIEL COMMAND
UNITED STATES AIR FORCE

NOTICE AND SIGNATURE PAGE

Using Government drawings, specifications, or other data included in this document for any purpose other than Government procurement does not in any way obligate the U.S. Government. The fact that the Government formulated or supplied the drawings, specifications, or other data does not license the holder or any other person or corporation; or convey any rights or permission to manufacture, use, or sell any patented invention that may relate to them.

This report is the result of contracted fundamental research deemed exempt from public affairs security and policy review in accordance with The Under Secretary of Defense memorandum dated 24 May 2010 and AFRL/DSO policy clarification email dated 13 January 2020. This report is available to the general public, including foreign nationals.

Copies may be obtained from the Defense Technical Information Center (DTIC) (http://www.dtic.mil).

AFRL-RY-WP-TR-2022-0269 HAS BEEN REVIEWED AND IS APPROVED FOR PUBLICATION IN ACCORDANCE WITH ASSIGNED DISTRIBUTION STATEMENT.

//Signature//

NICHOLAS G. USECHAK
Program Manager
Highly Integrated Microsystems Branch
Aerospace Components & Subsystems Division

//Signature//

STEPHEN L. HARYf
Chief
Highly Integrated Microsystems Branch
Aerospace Components & Subsystems Division

//Signature//

GENE M. WILKINS, Lt Col, USAF
Deputy Chief, Aerospace Components &
Subsystems Technology Division
Sensors Directorate

This report is published in the interest of scientific and technical information exchange, and its publication does not constitute the Government's approval or disapproval of its ideas or findings.

*Disseminated copies will show "//Signature//" stamped or typed above the signature blocks.

REPORT DOCUMENTATION PAGE

PLEASE DO NOT RETURN YOUR FORM TO THE ABOVE ORGANIZATION.

1. REPORT DATE	2. REPORT TYPE	3. DATES COVERED	
		START DATE	END DATE
November 2022	Final	12 January 2018	12 January 2021

4. TITLE AND SUBTITLE

DENSELY PACKED 2D PHOTONIC PHASED ARRAY USING SEMICONDUCTOR MONOLAYERS

5a. CONTRACT NUMBER	5b. GRANT NUMBER	5c. PROGRAM ELEMENT NUMBER
FA8650-18-1-7815	N/A	N/A
5d. PROJECT NUMBER	**5e. TASK NUMBER**	**5f. WORK UNIT NUMBER**
N/A	N/A	Y1QK

6. AUTHOR(S)

Ipshita Datta and Michal Lipson

7. PERFORMING ORGANIZATION NAME(S) AND ADDRESS(ES)

Columbia University
116TH and Broadway
New York, NY 10027

8. PERFORMING ORGANIZATION REPORT NUMBER

9. SPONSORING/MONITORING AGENCY NAME(S) AND ADDRESS(ES)		10. SPONSOR/MONITOR'S ACRONYM(S)	11. SPONSOR/MONITOR'SREPORT NUMBER(S)
Air Force Research Laboratory, Sensors Directorate Wright-Patterson Air Force Base, OH 45433-7320 Air Force Materiel Command, United States Air Forces	Defense Advanced Research Projects Agency (DARPA/MTO) 675 North Randolph Street Arlington, VA 22203	AFRL/RYDI	AFRL-RY-WP-TR-2022-0269

12. DISTRIBUTION/AVAILABILITY STATEMENT

DISTRIBUTION STATEMENT A. Approved for public release; distribution is unlimited.

13. SUPPLEMENTARY NOTES

This work was funded in whole or in part by Department of the Air Force contract FA8650-18-1-7815. The U.S. Government has for itself and others acting on its behalf an unlimited, paid-up, nonexclusive, irrevocable worldwide license to use, modify, reproduce, release, perform, display, or disclose the work by or on behalf of the U. S. Government. This material is based on research sponsored by the Air Force Research Lab (AFRL) and the Defense Advanced Research Projects Agency (DARPA) under agreement number FA8650-18-1-7815. The U.S. Government is authorized to reproduce and distribute reprints for Governmental purposes notwithstanding any copyright notation thereon. The views and conclusions contained herein are those of the authors and should not be interpreted as necessarily representing the official policies or endorsements, either expressed or implied, of the Air Force Research Labs (AFRL), the Defense Advanced Research Projects Agency (DARPA) or the U.S. Government. Report contains color.

14. ABSTRACT

This report was developed under a DARPA-funded contract. This effort explored technologies necessary to develop compact optical phased arrays by focusing on effective phase shifting using composite materials based on 2D materials.

15. SUBJECT TERMS

integrated optical phase shifters, integrated photonics, optical phased arrays, OPAs, LiDAR

16. SECURITY CLASSIFICATION OF:			17. LIMITATION OF ABSTRACT	18. NUMBER OF PAGES
a. REPORT	b. ABSTRACT	C. THIS PAGE		
Unclassified	Unclassified	Unclassified	SAR	44

19a. NAME OF RESPONSIBLE PERSON	19b. PHONE NUMBER *(Include area code)*
Nicholas Usechak	

PREVIOUS EDITION IS OBSOLETE.

STANDARD FORM 298 (REV. 5/2020)
Prescribed by ANSI Std. Z39.18

Table of Contents

List of Figures

Figures **Page**

1 SUMMARY

This effort explores the use of two dimensional (2D) materials to create compact, high-performance, low-loss optical modulators. 2D materials such as graphene and transition metal dichalcogenides (TMDs) are finding applications in optical modulation, detection, and light emission since their optical properties can be electrically tuned by modifying their carrier densities [1,2]. To date the electro-optic properties have been probed near their excitonic resonances, where the optical propagation loss is prohibitively high for large-scale photonic applications. In contrast with thse prior investigations, this work explores the strong electro-refractive response of monolayer TMDs at near infrared wavelengths by placing the monolayer on a low-loss planarized silicon nitride (SiN) photonic structure. We dope the monolayer with carrier densities of $(7.2 \pm 0.8) \times 10^{13}$ cm^{-2} by electrically gating the TMD using an ionic liquid ([P14^{+}] [FAP^{-}]). We measure a large change in the real part of the refractive index, $\Delta n = 0.53$, with only a minimal change in the imaginary part ($\Delta k = 0.004$). We further demonstrate photonic devices based on an electrostatically gated SiN–WS_2 phase modulator with a high efficiency ($V_\pi L$) of 0.8 V cm. These efficient phase modulators exhibit a large $|\Delta n/\Delta k|$ but offer low propagation losses which are critical for enabling large-scale photonic systems for applications such as light detection and ranging (LiDAR), phased arrays, optical switching, coherent optical communications, quantum applications, and optical neural networks.

We further describe a novel platform for electrically reconfiguring the coupling between a bus waveguide and ring resonator to design an ultra-compact, low-loss, low-power and high-speed phase shifter, based on a combination of the strong electro-refractive response in monolayer TMDs. In this case we focus on WS_2 and the strong electro-absorptive property of graphene. Nevertheless, this approach is general and inclusive of all TMD semiconductors including but not limited to MoS_2, WSe_2, $MoSe_2$, WSe_2, and $MoTe_2$. We show that our 25-μm long WSe_2-graphene-based silicon nitride (SiN) composite waveguide, when embedded in a ring resonator configuration, offers an analog optical phase modulation of π/2 with an amplitude modulation of only 2 dB, accompanied with an insertion loss of 3 dB and a 3-dB electro-optic bandwidth of 15 GHz. We further show that this platform is capable of performing differential phase shift keying (DPSK), where the phase of the optical signal can switch between 0 and π radians with no amplitude modulation and an insertion loss of 5 dB.

2 INTRODUCTION

2.1 Electro-optic Properties of Semiconductor Monolayers

Transition metal dichalcogenides (TMDs) belong to a class of semiconductor monolayers with a direct bandgap at visible wavelengths. The strong susceptibility of the optical properties of monolayer semiconductor TMDs with doping renders them ideal for a variety of opto-electronic applications. Their natural surface passivation and strong light-matter interaction allows for easy integration with passive waveguides which turns them into active composite structures [3,4]. Recently, TMDs such as tungsten disulphide (WS_2) and molybdenum disulphide (MoS_2) have been shown to exhibit strong changes in their optical properties with doping [5–7]. However, these measurements have historically been performed near the optical bandgap of the TMDs (i.e. near excitonic resonances), where the optical propagation loss is prohibitively high for many photonic applications [8]. Here, we investigate the effect of doping on the electro-optic properties of TMDs at wavelengths in the transparency regime using in-plane, low-loss, silicon nitride (SiN) waveguides.

We demonstrate that monolayer TMDs experience a strong electro-refractive response with induced carrier densities when probed in the near-infrared (NIR) wavelength region. In order to probe the doping-induced electro-optic response of TMDs, we integrate monolayer TMD such as WS_2 on planarized low-loss SiN waveguides embedded in a microring resonator cavity configuration, as illustrated in Figure 1a. Microring resonators provide enhanced sensitivities to small changes in phase and absoprpiton due to their high Q factors ($Q_{loaded} \sim 123{,}000$ in our case). Our planar photonic structure is comprised of a SiN-TMD composite waveguide, which allows enhanced optical mode interaction with the monolayer when compared to out-of-plane measurements. We develop the SiN-TMD platform by using standard fabrication techniques to define a 1.3-μm wide × 330-nm tall low-pressure chemical vapor deposition (LPCVD) SiN waveguide clad with 100 nm of plasma-enhanced chemical vapor deposition (PECVD) SiO_2 and embedded in a microring resonator with a 50-μm ring radius. This is followed by patterning a 30-μm long metal-organic chemical vapor dpeposition (MOCVD) grown monolayer TMD on the SiN waveguide followed by the deposition of metal contacts (Ti/Au) to gate the TMD.

We leverage the SiN-WS_2 platform to characterize the electro-optic response (i.e. the index change) of the monolayer WS_2 ($\Delta n WS_2 + i\Delta k WS_2$) by tuning the complex effective index ($\Delta n\text{eff} + i\Delta k\text{eff}$) of the composite mode. We tune the effective index by doping the WS_2 using an ionic liquid ([$P14^+$] [FAP^-]). We use the ionic liquid [P14+] [FAP-] in our experiments due to its stability to gating under atmospheric exposure at room temperature. One can see from Figure 1b, that we dope the monolayer by applying a potential difference between the two electrodes. This results in the accumulation of ions at the surface of the WS_2, which introduces image charges into the monolayer. The maximum electron doping density induced in the monolayer is about 6.44×10^{13} cm^{-2} with an applied voltage of 2 V. The charge density in ionic liquid-gated devices is dominated by the quantum capacitance (Cq) as predicted by D. Braga *et al.* [9]. One can see from the mode cross-section in the inset of Figure 1b, that the optical mode is shared between the monolayer and the SiN waveguide. We estimated an optical mode overlap of 0.06% based on simulations perfomered using COMSOL Multiphysics.

Figure 1c shows the measured transmission spectrum of the ring resonator as a function of voltage. The cavity has a narrow linewidth resonance near 1571.55 nm confirming that the incorporation of WS_2 introduces negligible loss and does not degrade the quality factor of the microring resonator. At positive gate voltages above 1 V we observe a redshift in the resonance wavelength which indicates an increase in the effective index of the resonator. Remarkably, the resonance linewidth is largely unchanged, showing that doping does not introduce substantial loss. The measured changes in resonance wavelength and quality factor with applied voltage can be used to derive the changes in real and imaginary components of the effective index (Δn_{eff} and Δk_{eff}, respectively) of the composite waveguide. We measure a maximum effective index change (Δneff) of 6.6×10^{-4} in refractive index units (RIU) with a change in absorption ($\Delta\alpha$) of 4.5 dB/cm for a voltage swing of 2 V. We extract the Δneff and $\Delta\alpha$ from the normalized transmission spectra of the ring resonator for different voltages applied across the Ti/Au electrodes, as shown in figure 1c.

We show a large electro-refractive response at NIR wavelengths by estimating a maximum change of 0.53 ± 0.06 RIU in the real ($\Delta n WS_2$) and 0.004 ± 0.002 in the imaginary part (ΔkWS2) of the refractive index of the WS_2 monolayer for electron doping densities of 6.44×10^{13} cm^{-2}. We extract the index of monolayer WS_2 by comparing the measured effective index of the SiN-WS_2 composite mode with the COMSOL simulated change, which we obtained by modelling the monolayer as a 2D sheet with optical conductivity σ_S integrated on a SiN waveguide. In Figure 1d, we show the extracted change in the ΔnWS_2 and ΔkWS_2 as a function of charge carrier density in the monolayer WS_2. One can see that the electro-refractive response (ΔnWS_2) for monolayer WS_2 is about two orders of magnitude stronger than its electro-absorptive response (ΔkWS_2) at NIR wavelengths which indicates that the propagating light undergoes significant phase change with low optical loss. The physical mechanism for the strong electro-refractive effect remains to be studied in detail. Due to the Lorentzian nature of the dielectric response in monolayer TMDs [10], the excitonic resonances contribute to the real part of the dielectric function over a much larger frequency band than their effect on the imaginary part. Thus, doping-dependent tuning of multiple strong excitonic resonances will lead to a high $|\Delta n/\Delta k|$ in the transparency regime. The free-carrier plasma dispersion predicted via a Drude model can also lead to a similar effect due to the comparable larger conductivity effective mass in TMD monolayers [11–13]. Additionally, the 2D configuration of monolayer TMDs in the composite platform lends itself to extremely high doping of the material.

Figure 1e shows that the doping induced $|\Delta n/\Delta k| \sim 125$ for semiconductor monolayers at NIR wavelengths is higher than the $|\Delta n/\Delta k|$ reported for graphene (~3.5) [14–17], monolayer WS_2 and MoS_2 when probed at their excitonic resonance (~1 at 0.64 μm) [8,18], or traditional bulk materials such as silicon (Si) (~10–30) [19–22]. Here we present a comparison between the carrier-induced $|\Delta n/\Delta k|$ (a key metric for photonics) and the propagation length ($L = 1/\alpha$, where α is insertion loss in 1/μm) for various 2D and bulk electro-refractive materials such as Si and III-V on Si [23]. The propagation length (L) is characterized as the length in which the propagating optical field decays by 1/e and can be expressed as $L = 1/\alpha$, where α (insertion loss) $= 4\pi\,(k(\lambda) \pm \Delta k)/\lambda$, $k(\lambda)$ is the imaginary part of the effective index, $\pm\,\Delta k$ is the change in the imaginary part of the effective index and λ denotes the wavelength.

Figure 1c shows the measured transmission spectrum of the ring resonator as a function of voltage. The cavity has a narrow linewidth resonance near 1571.55 nm confirming that the incorporation of WS_2 introduces negligible loss and does not degrade the quality factor of the microring resonator. At positive gate voltages above 1 V we observe a redshift in the resonance wavelength which indicates an increase in the effective index of the resonator. Remarkably, the resonance linewidth is largely unchanged, showing that doping does not introduce substantial loss. The measured changes in resonance wavelength and quality factor with applied voltage can be used to derive the changes in real and imaginary components of the effective index (Δn_{eff} and Δk_{eff}, respectively) of the composite waveguide. We measure a maximum effective index change (Δneff) of 6.6×10^{-4} in refractive index units (RIU) with a change in absorption ($\Delta\alpha$) of 4.5 dB/cm for a voltage swing of 2 V. We extract the Δneff and $\Delta\alpha$ from the normalized transmission spectra of the ring resonator for different voltages applied across the Ti/Au electrodes, as shown in figure 1c.

Figure 1c shows the measured transmission spectrum of the ring resonator as a function of voltage. The cavity has a narrow linewidth resonance near 1571.55 nm confirming that the incorporation of WS_2 introduces negligible loss and does not degrade the quality factor of the microring resonator. At positive gate voltages above 1 V we observe a redshift in the resonance wavelength which indicates an increase in the effective index of the resonator. Remarkably, the resonance linewidth is largely unchanged, showing that doping does not introduce substantial loss. The measured changes in resonance wavelength and quality factor with applied voltage can be used to derive the changes in real and imaginary components of the effective index (Δn_{eff} and Δk_{eff}, respectively) of the composite waveguide. We measure a maximum effective index change (Δneff) of 6.6×10^{-4} in refractive index units (RIU) with a change in absorption ($\Delta\alpha$) of 4.5 dB/cm for a voltage swing of 2 V. We extract the Δneff and $\Delta\alpha$ from the normalized transmission spectra of the ring resonator for different voltages applied across the Ti/Au electrodes, as shown in figure 1c.

We show a large electro-refractive response at NIR wavelengths by estimating a maximum change of 0.53 ± 0.06 RIU in the real ($\Delta n WS_2$) and 0.004 ± 0.002 in the imaginary part (ΔkWS2) of the refractive index of the WS_2 monolayer for electron doping densities of 6.44×10^{13} cm^{-2}. We extract the index of monolayer WS_2 by comparing the measured effective index of the SiN-WS_2 composite mode with the COMSOL simulated change, which we obtained by modelling the monolayer as a 2D sheet with optical conductivity σ_S integrated on a SiN waveguide. In Figure 1d, we show the extracted change in the $\Delta n WS_2$ and $\Delta k WS_2$ as a function of charge carrier density in the monolayer WS_2. One can see that the electro-refractive response ($\Delta n WS_2$) for monolayer WS_2 is about two orders of magnitude stronger than its electro-absorptive response ($\Delta k WS_2$) at NIR wavelengths which indicates that the propagating light undergoes significant phase change with low optical loss. The physical mechanism for the strong electro-refractive effect remains to be studied in detail. Due to the Lorentzian nature of the dielectric response in monolayer TMDs [10], the excitonic resonances contribute to the real part of the dielectric function over a much larger frequency band than their effect on the imaginary part. Thus, doping-dependent tuning of multiple strong excitonic resonances will lead to a high $|\Delta n/\Delta k|$ in the transparency regime. The free-carrier plasma dispersion predicted via a Drude model can also lead to a similar effect due to the comparable larger conductivity effective mass in TMD

monolayers [11–13]. Additionally, the 2D configuration of monolayer TMDs in the composite platform lends itself to extremely high doping of the material.

Figure 1e shows that the doping induced $|\Delta n/\Delta k| \sim 125$ for semiconductor monolayers at NIR wavelengths is higher than the $|\Delta n/\Delta k|$ reported for graphene (~3.5) [14–17], monolayer WS_2 and MoS_2 when probed at their excitonic resonance (~1 at 0.64 μm) [8,18], or traditional bulk materials such as silicon (Si) (~10–30) [19–22]. Here we present a comparison between the carrier-induced $|\Delta n/\Delta k|$ (a key metric for photonics) and the propagation length ($L = 1/\alpha$, where α is insertion loss in 1/μm) for various 2D and bulk electro-refractive materials such as Si and III-V on Si [23]. The propagation length (L) is characterized as the length in which the propagating optical field decays by 1/e and can be expressed as $L = 1/\alpha$, where α (insertion loss) $= 4\pi (k(\lambda) \pm \Delta k)/\lambda$, $k(\lambda)$ is the imaginary part of the effective index, $\pm \Delta k$ is the change in the imaginary part of the effective index and λ denotes the wavelength.

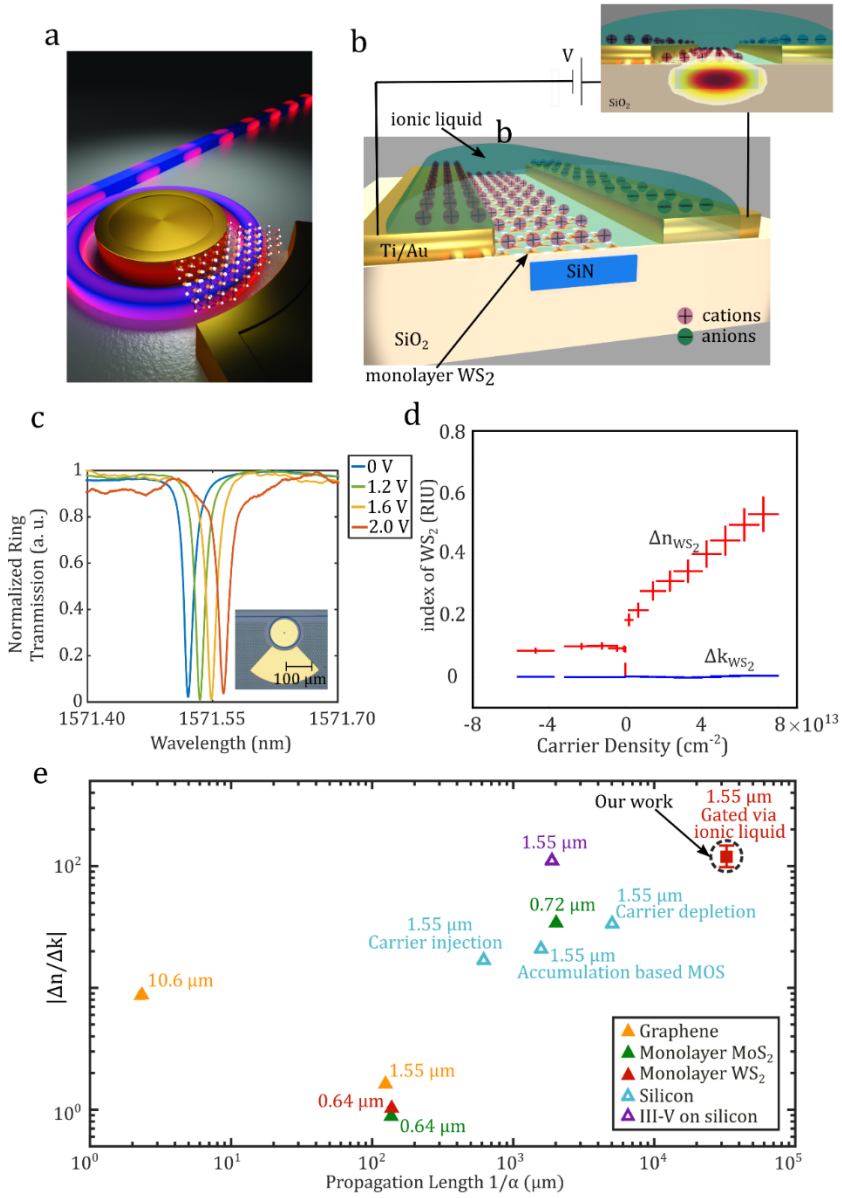

Figure 1: Electro-optic Properties of Semiconductor Monolayer TMDs

(a) Diagrammatic illustration of a microring resonator with patterned TMD and electrodes for doping. (b) Cross-section of the composite SiN-monolayer WS_2 waveguide with ionic liquid ([$P14^+$] [FAP^-]) cladding. The monolayer WS_2 is doped by applying a bias (V) across the two electrodes, through the ionic liquid, resulting in the accumulation of charged carriers at the interface with the WS_2. Top inset: TE mode profile of the propagating mode, indicating 0.06% mode overlap with the monolayer TMD. (c) Normalized transmission response of the microring resonator with different voltages applied across the electrodes immersed in the ionic liquid. (d) Change in the real and imaginary part of the refractive index of monolayer WS_2 with induced carrier densities. One can see that the Δn_{WS2} changes two orders of magnitude faster than Δk_{WS2}, thereby indicating the combination of strong electro-refractive response accompanied with low propagation loss. (e) Comparison of $|\Delta n/\Delta k|$ versus the optical propagation loss of TMD monolayers at NIR wavelengths with graphene and bulk materials such as silicon and III-V on silicon.

2.1.1 Polarizability of the Electro-refractive Response in Monolayer TMDs

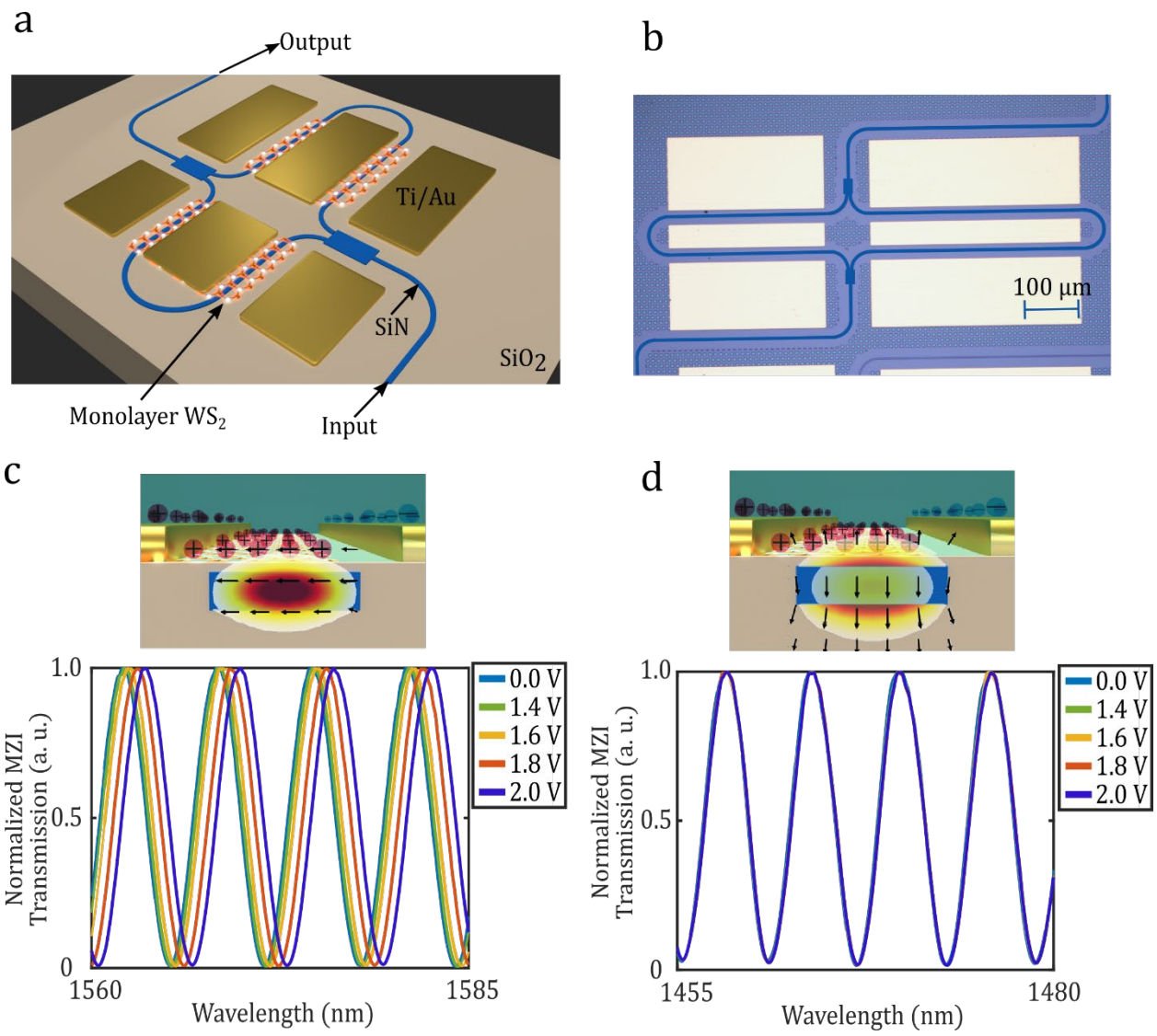

Figure 2: Polarization-dependent index change in monolayer WS_2.
Diagrammatic illustration of an on-chip Mach–Zehnder interferometer (MZI) with patterned monolayer WS_2 on the longer arm of the MZI. The monolayer is doped by applying a bias voltage across the two electrodes, after dispersing 3-4 µL of ionic liquid ([P14+] [FAP-]). (b) Optical micrograph of the fabricated MZI with SiN-WS_2 waveguides (false-colored), before ionic liquid is dispersed on the devices. (c) Normalized Transmission response of the MZI for the optical TE mode at different voltages applied across the two electrodes located on the longer arm of the MZI. One can see that the MZI transmission spectra exhibit fringes due to the path length difference between the two arms of the MZI, which red shifts with applied voltage. The top inset shows the optical mode profile for the mode, with the arrows illustrating the field lines aligned with the plane of monolayer WS_2. (d) Normalized transmission response of the MZI for the optical TM mode at different voltages. The top inset dhows the optical mode profile for the TM mode with the optical field lines perpendicular to the plan of monolayer WS_2.

We confirm that the phase change due to the monolayer occurs only when the electric field of the propagating light is in plane with the monolayer (i.e. the optical TE mode) by embedding the monolayer WS2 on SiN waveguides in a Mach–Zehnder interferometer (MZI) configuration (see Figure 2a). Figure 2b shows the optical micrograph of the fabricated MZI device. The MZI is designed with a length imbalance of 200 μm between the two arms such that the transmission spectra exhibit clear fringes in the wavelength range spanning from 1560 to 1585 nm for the TE mode (see Figure 2c) and 1455 to 1480 nm for the TM mode (see Figure 2d). The power splitter (combiner) at the input (output) of the MZI structure is designed using a 1×2 (2×1) multimode interferometer (MMI). Our MZI operates at different wavelengths for both optical TE and TM modes due to the aspect ratio of the height-to-width (330 to 1,300 nm) of the waveguide and the MMI structure which supports TM mode at lower wavelengths compared to the TE mode. A 500-μm long monolayer WS2 is patterned on the longer arm of the MZI with the monolayer in contact with one of the electrodes while the other electrode acts as a gate to dope the monolayer through the ionic liquid [P14+] [FAP-] (see Figure 1b).

2.1.2 Electro-optic Properties of Monolayer Graphene

Graphene is a versatile 2D material which posseses a wavelength-insensitive electrical tunability of its optical absorption and refractive index (Figure 3). The optical properties of 2D graphene can be modified electrically as described by theoretical models [24,25]. Graphene operates in two regimes:

(I) the normal regime where both the real and imaginary part of the refractive index (RI) tune simultaneously (i.e. the Pauli blocking regime where inter-band absorption dominates) and

(II) (II) the anomalous regime, where the real part of the refractive index (RI) can be tuned without altering the imaginary part (i.e. absorption) above the Pauli blocking limit, where intraband absorption dominates.

Importantly, the optical properties of graphene can be tuned by "doping" the graphene electrostatically, i.e. by applying a voltage V across a graphene-insulator-graphene capacitor. One can see from the theory in Figure 3, that in region I, the absorption in monolayer graphene is lowered with doping, and the index changes strongly. As the Fermi level is tuned beyond the inter-band absorption limit, the absorption becomes negligible, while the index of refraction changes drastically.

To date, state-of-the-art electro-optic graphine-based modulators have been predominatly designed to operate in region I, where the absorption and index can be tuned together. This is partly due to the fact that the doping densities required to operate in regime II are extremely high and require a high K dielectric.

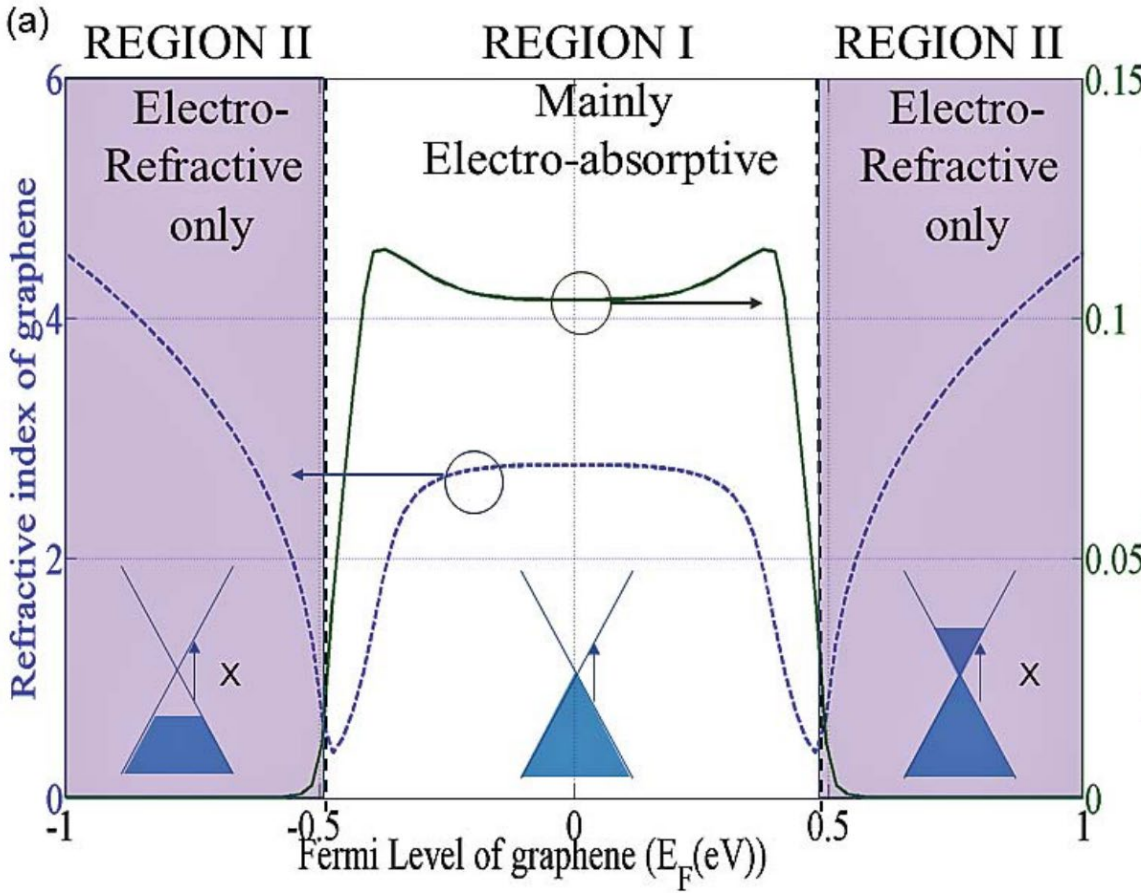

Figure 3: Electro-optic properties of graphene.
(a) Theoretical absorption and refractive index as a function of Fermi level for intrinsic graphene. Region I depicts the normal regime which is characterized by high absorption (both absorption and index tune simultaneously). Region II is known as the anomalous regime and is characterized by low absorption (the refractive index changes strongly compared to the absorption).

2.1.3 SiN-TMD Capacitive Platform for Low-loss Broadband Phase Modulator

The fundamental optical loss associated with phase modulation in today's silicon photonics limits the scalability of emerging large-scale systems including light detection and ranging (LiDAR), quantum circuits, optical neural networks and optical communication links [26–30]. This loss occurs because traditional silicon phase modulators such as PN, PIN, MOS and III-V on silicon rely on changes in the carrier concentration, which changes not only the real part of the refractive index but also the imaginary part (see figure 1e). Today this optical loss is reduced by decreasing the carrier concentration required for modulation using long devices, thereby limiting the scalability of these systems. Phase modulators based on either thermo-optic or induced electro-optic $\chi(2)$ effects have low optical losses but suffer from either high electrical power consumption [31–33] or require a large device footprint and complex fabrication [34,35], respectively.

In this work, we demonstrated a platform that enables phase-only modulation in the NIR region of the electromagnetic spectrum based on monolayer TMD integrated on passive silicon nitride waveguides (see figure 4). To leverage the doping-induced strong electro-refractive response in monolayer TMDs for photonic applications, we have developed a fully integrated SiN-TMD capacitive platform that gates the monolayer TMD using a parallel plate capacitor configuration. We replace the ionic liquid with a stack of Hafnia oxide (HfO_2) and indium tin oxide (ITO) to form the TMD-HfO_2-ITO capacitor on the SIN waveguide (Figure 4a). Standard processes are used to define the 1,000 × 360 nm LPCVD SiN waveguide, clad with 260 nm of SiO_2. We replaced the MOCVD-grown monolayer WS_2 used in the ionic liquid experiments with CVD-grown films for the capacitive devices [36].

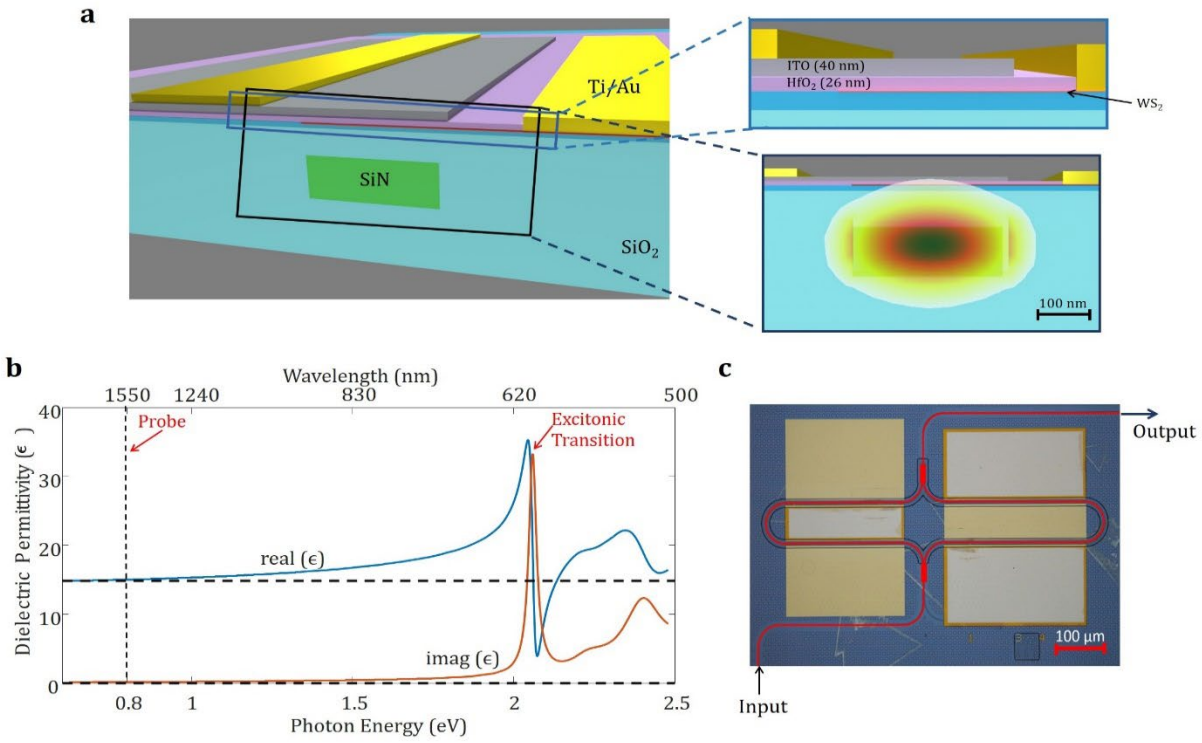

Figure 4: Schematic of the SiN-TMD Capacitive Platform for Pure Phase Modulation
(a) Illustration of a composite SiN-monolayer TMD (WS_2) waveguide, where the optical mode is shared between the SiN waveguide and the WS_2. The inset details the WS_2-HfO_2-ITO parallel plate capacitor configuration which gates the monolayer WS_2 by applying a bias voltage across the dielectric HfO_2. (b) The real (Re[ϵ]) and imaginary (Im[ϵ]) part of the dielectric permittivity (ϵ) of the monolayer WS_2 are modeled using the parameters extracted from Li et. al. [10]. The strong excitonic transition at 620 nm in Im[ϵ] decays rapidly with increase in wavelength and is negligible at the probe wavelength of 1550 nm. On the other hand, the excitonic feature in Re[ϵ] decays more slowly with wavelength and retains significant excitonic contributions at the probe wavelength. (c) Optical micrograph of the fabricated phase modulator consisting of the composite SiN WS_2 waveguide shown in (a) embedded in the two arms (false-colored) of an unbalanced MZI.

2.1.3.1 Principle of operation

We induce phase tuning in the composite SiN-WS_2 waveguide by taking advantage of the fact that the excitonic transitions in monolayer TMDs are sensitive to gating. These excitonic transitions have a strong oscillator strength, which contributes to the dielectric permittivity of the monolayer WS_2 across a wide spectral range. In figure 4b, we plot the real (Re[ϵ]) and imaginary (Im[ϵ]) components of the dielectric permittivity for monolayer WS_2 using the parameters extracted from Li et al [31]. One can see that the strong excitonic transition at 620 nm in Im[ϵ] decays much faster than the Re[ϵ] part with an increase in wavelength. In order to achieve "lossless" modulation, we probe the phase change in monolayer WS_2 at NIR wavelengths (~1550 nm), well removed from the excitonic transition. In this regime, Re[ϵ] retains contributions from the excitonic transitions that can be modified by gating, while the excitonic contribution to Im[ϵ], which causes optical absorption, is negligible. This is in strong contrast to the dielectric permittivity at visible wavelengths near the excitonic transition, where both Re[ϵ] and Im[ϵ] are susceptible to gating-induced changes in the excitonic resonances.

2.1.4 Principle of operation

Microring resonators have revolutionized silicon photonics and are frequently used as intensity modulators in a host of applications [37]. Microring resonators operating in the critical coupling regime enhance small changes in the waveguide response as they increase the effective propagation length of the optical mode with the finesse with the cavity. However, ring resonators have not been used to amplify the phase response. This is because the phase and amplitude in a resonator are intrinsically linked to one another through the Kramers–Kronig relation — such that at resonance (i.e. maximum extinction) the system is highly dispersive and transmission is minimal. In order to leverage ring resonators in this work, we designed a hybrid waveguide where we can modulate both loss and index in the ring resonator similar amounts. Figure 4a shows the concept of using a combination of index and loss change in a ring resonator configuration to achieve strong phase modulation with minimal amplitude modulation, while simultaneously maintaining low insertion loss. One can see from the theoretical simulation in figure 4b, that by tuning the loss in the ring resonator, one can change the coupling condition between the bus waveguide and ring resonator from the under-coupled to the over-coupled regime. This is accompanied by a shift in resonance wavelength due to the index change. In such a regime, at a probe wavelength defined by the purple dashed lines in figure 4b, the phase can be altered by π radians with low insertion losses and minimal amplitude modulation.

In order to tune the loss/index of the effective propagating mode, we leverage the electro-optic properties of monolayer graphene and monolayer WSe_2 and embed the 2D materials on a 1,300 nm wide × 330 nm tall SiN waveguide covered with 210 nm of silicon dioxide (SiO_2). In so doing we allow for the optical mode to overlap partially with both the monolayers (as seen in top image of figure. 4d). We inject charges into the monolayers by applying a voltage across the 40-nm thick Al_2O_3 dielectric ($\varepsilon_R = 6.3$) separating the WSe_2 and graphene monolayers (figure 4c). At lower doping densities the change in absorption due to graphene is stronger compared to the index change, whereas at higher doping densities the change in the index due to ambipolar TMD (WSe_2) supersedes the absorption change. This is in contrast to the electro-optic response of traditional electro-refractive materials such as bulk silicon, where both the absorption and index increases in conjunction with doping. Due to the capacitive nature of the electro-optic device, the DC power consumption in these devices is limited to a few nanowatts, and the speed

of operation exceeds 15 GHz and is primarily limited by the contact resistance between the monolayers TMD and metallic contact pads (Ti/Pd/Au).

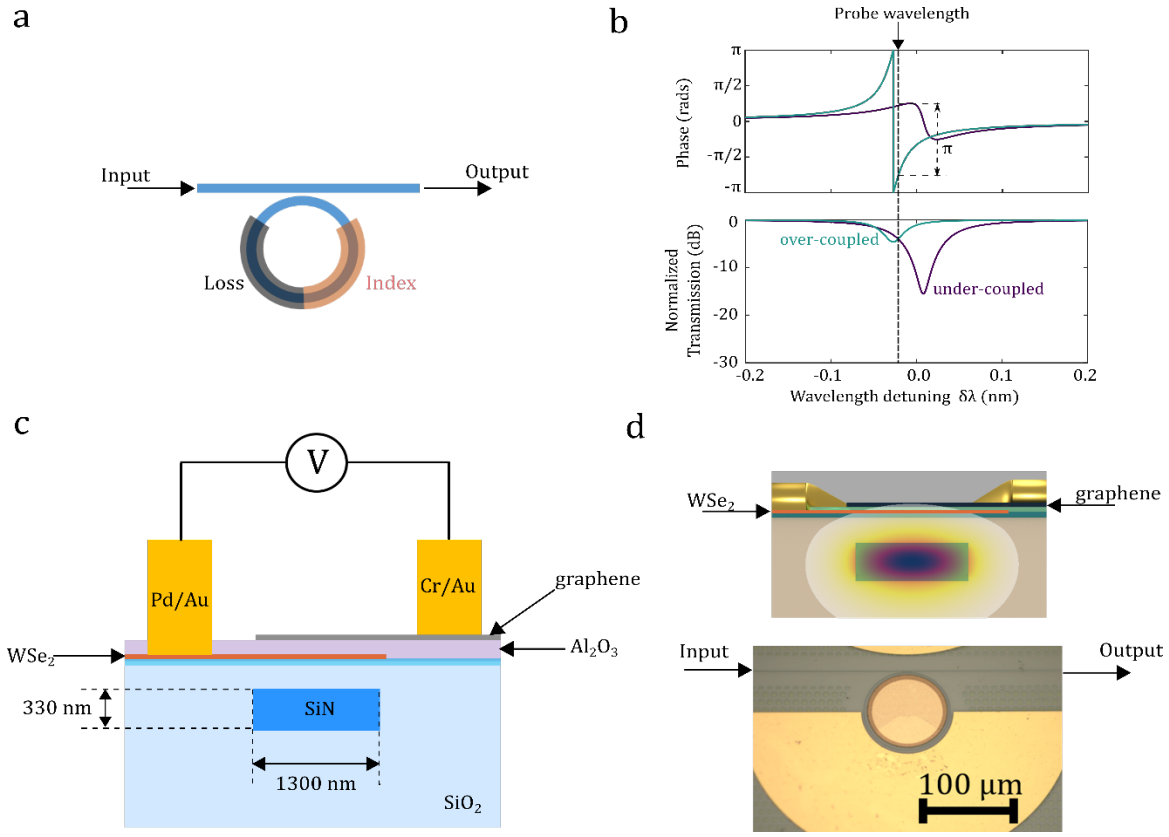

Figure 5: Principle of Operation and Design of TMD (WSe_2) – Graphene Composite Platform for Pure Phase Modulation

(a) Schematic representation of a bus waveguide coupled to a microring resonator, where the loss (grey) and index (orange) in the ring resonator is modulated simultaneously. (b) Theoretically computed phase response (top panel) and normalized ring transmission (bottom panel) at the output of the ring resonator when both the index and loss of the cavity is modulated simultaneously. One can see that tuning the loss in the cavity changes the coupling condition between the bus waveguide and ring resonator, from the under-coupled (purple) to the over-coupled regime (green), whereas tuning the index causes a shift in the resonance wavelength. By leveraging both the loss dependent coupling change and the index dependent resonance wavelength shift, one can achieve an abrupt phase change of π radians at the designed probe wavelength with insignificant amplitude modulation while maintaining a low insertion loss. (c) Device cross-section showing a TMD (WSe_2)-Al_2O_3-graphene capacitor on a 1300-nm wide × 330-nm tall SiN waveguide. (d) Top panel indicates the position of monolayer WSe_2 and graphene in the mode profile of the SiN waveguide cross section. The bottom panel shows the optical micrograph of the fabricated device with a 25-μm long WSe_2-Al_2O_3-graphene capacitor embedded in a 50-μm radius ring resonator.

In the next section we introuduce our theoriteical framkework for understanding the experimantatl results obtained in this work.

3 METHODS, ASSUMPTIONS, AND PROCEDURES

3.1 Calculation of Δn_{eff} and Δk_{eff} for Ionic Liquid clad SiN-WS_2 Rings

We calculate the change in the real/imaginary part of the effective index ($\Delta n_{\text{eff}}/\Delta k_{\text{eff}}$) of the propagating mode with varying voltage from the change in the resonance wavelength/quality factor (Q) associated with the normalized transmission response of a ring resonator critically coupled to a bus waveguide. We numerically fit the normalized experimental ring transmission to the theoretical ring transmission (T) obtained using equation (1) [38].

$$\mathrm{T} = \left|\frac{b_1}{a_1}\right|^2 = \left|\frac{t - \alpha e^{j\Theta}}{1 - \alpha t^* e^{j\Theta}}\right|^2 \tag{1}$$

where, t is the transmission factor, the linear loss is defined by $\alpha = e^{-j\frac{2\pi}{\lambda}k_{\text{eff}}L}$, the phase $\Theta = \frac{2\pi}{\lambda} n_{\text{eff}} L$ and $L = 2\pi R$, where R is the radius of the ring resonator (R = 60 μm). Since the change in the effective index of the mode is concentrated only in the length of the ring with monolayer WS2 (L_{WS2}), the phase $\Theta = \frac{2\pi}{\lambda} n_{\text{eff}_{\text{SiN}}}(L - L_{\text{WS2}}) + \frac{2\pi}{\lambda} n_{\text{eff}_{\text{WS2}}}(\mathrm{V})\, L_{\text{WS2}}$, where $n_{\text{eff}_{\text{SiN}}}$ is the effective index of the SiN ring resonator without WS_2 and $n_{\text{eff}_{\text{WS2}}}(\mathrm{V})$ is the voltage dependent effective index of the SiN waveguide interacting with monolayer WS_2. At the resonance wavelength, the transmission through the bus waveguide experiences a minimum, indicating that the phase Θ = 2mπ$2m\pi$. In order to extract the Δn_{eff} from the normalized transmission spectra, we track the evolution of the change in the resonance wavelength ($\Delta\lambda_{res}\Delta\lambda_{\text{res}}$) with voltage and use equations (2) and (3).

$$m(\lambda_{\text{res}}(\mathrm{V}) - \lambda_{\text{res}}(\mathrm{V}=0)) = \Delta n_{\text{eff}_{\text{WS2}}}(\mathrm{V}) L_{\text{WS2}} \tag{2}$$

$$\Delta n_{\text{eff}_{\text{WS2}}}(\mathrm{V}) = n_{\text{eff}_{\text{WS2}}}(\mathrm{V}) - n_{\text{eff}_{\text{WS2}}}(\mathrm{V}=0) \tag{3}$$

To extract $\Delta k_{eff}\Delta k_{\text{eff}}$, we first use equation (2) to find the $\Delta n_{eff\_WS2} n_{\text{eff}_{\text{WS2}}}(\mathrm{V})$ and then use MATLAB to curve fit the result with equation (1) to track the evolution of α as a function of applied voltage.

3.1.1 Optical Sheet Conductivity of Monolayer TMD

For monolayer films, the optical sheet conductivity $[\sigma_s(\omega)]$ provides a full description of the optical response and is related to the dielectric permittivity $[\varepsilon_r(\omega)]$ through the equation

$$\sigma_s(\omega) = -j\omega t_d \varepsilon_0 \left(\varepsilon_r(\omega) - 1\right) \tag{4}$$

where, t_d defines the thickness of the monolayer TMD (0.8 nm). We model the monolayer TMD as a sheet with complex optical conductivity $\sigma_s = \sigma_R + j\sigma_I$. The change in the real part of the mode's effective index (Δn_{eff}) signifies a change in the imaginary part of the optical conductivity ($\Delta\sigma_I$), whereas the change in the absorption (Δα) of the mode is reflected in the real part of the optical conductivity ($\Delta\sigma_R$) through equation (4). Since the change in complex effective index of the composite SiN-WS_2 waveguide is contingent on the spatial overlap between the propagating optical mode and the monolayer WS_2, the true measure of the efficiency

of the phase modulation lies in the change of its in-plane optical sheet conductivity (σ_S) with electrostatic gating. We calculate the $\Delta\sigma_I$ of the monolayer WS_2 by modeling the monolayer as a boundary condition with surface current density ($J = \sigma_s \cdot E$) in COMSOL which eliminates the need to approximate the monolayer thickness. The extracted $\Delta\sigma_R$ is within the error limits of our COMSOL simulation, due to the minimal change in $\Delta\alpha$ with gating. We use the 2D sheet conductivity model to extract the Δn_{WS2} and Δk_{WS2}, as is commonly done when modeling graphene monolayers [39]. We extract the complex index change of the monolayer ($\Delta n + i\Delta k$) with carrier densities by comparing the measured Δn_{eff} and Δk_{eff} with the simulated change obtained using COMSOL Multiphysics finite element model (FEM). We model the monolayer TMD as a conductive sheet with a surface charge density ($J = \sigma_s \cdot E$) and complex optical conductivity [10] $\sigma_s = \sigma_R + j\sigma_I$. Here $\sigma_s(\omega)$ is related to the dielectric permittivity [$\varepsilon(\omega)$] through the equation

$$\sigma_s(\omega) = j\omega t_d \varepsilon_0 \, (\varepsilon(\omega) - 1), \tag{5}$$

where t_d defines the thickness of the monolayer TMD (0.85 nm ± 0.05 nm) [8]. We estimate the complex index change of the monolayer from the computed change in conductivity ($\Delta\sigma$) using the equation

$$\sigma_s(\omega) + \Delta\sigma = j\omega t_d \varepsilon_0 \, (\varepsilon(\omega) + \Delta\varepsilon - 1) \tag{6}$$

Where, $\Delta\varepsilon$ defines the change in dielectric permittivity ($\varepsilon(\omega)$), which is related to Δn and Δk through

$$\varepsilon(\omega) + \Delta\varepsilon = (n + \Delta n + i(k + \Delta k))^2. \tag{7}$$

We quantify the mode overlap by replacing the surface current density ($J = \sigma \cdot E$) in the conductivity calculation with a surface of 0.8 nm thickness, and then find the surface integral of the energy flux ($E \times H$) of the mode in monolayer WS_2 and compare it to the total mode flux in the composite waveguide.

3.1.2 Optical Sheet Conductivity of Graphene

The optical properties of 2D graphene can be modified electrically and, according to theory [24,25], the real part of the refractive index (RI) can be tuned without altering the imaginary part (i.e. absorption). The optical properties of graphene can be tuned by doping graphene electrostatically, i.e. by applying a voltage V across a graphene-insulator-graphene capacitor. The doping of graphene induces a shift in the Fermi energy level of graphene and is given by:

$$E_F = \hbar v_F \left(\left(\frac{\epsilon_0 \epsilon_R V}{de} + n_{initial} \right) \pi \right)^{1/2}, \tag{1}$$

where ϵ_0 is the vacuum permittivity, ϵ_R is the relative permittivity of the insulator, e is the electronic charge, v_F is the Fermi velocity in graphene, and $n_{initial}$ is the initial chemical doping of the graphene layer (which is dependent on the processing of the graphene and on the substrate [40,41]). The real part (n_R) and imaginary part (n_I) of the RI of graphene are related to the optical conductivity $\sigma(\omega)$ through equations 2 and 3 [24,25] ;

$$(n_R + in_I)^2 = 1 + \frac{i\sigma(\omega)}{\hbar\omega t} \tag{2}$$

$$\sigma(\omega) = \frac{\sigma_0}{2}\left(tanh\frac{\hbar\omega + 2E_F}{4k_BT} + tanh\frac{\hbar\omega - 2E_F}{4k_BT}\right) - i\frac{\sigma_0}{2\pi} log\left[\frac{(\hbar\omega + 2E_F)^2}{(\hbar\omega - 2E_F)^2 + (2k_BT)^2}\right] + i\frac{4\sigma_0}{\pi}\frac{E_F}{\hbar\omega + i\frac{\hbar}{\tau}}, \tag{3}$$

where t is the thickness of the graphene layer (0.345 nm), σ_0 is the universal conductivity of graphene, $\hbar$ is the reduced Planck's constant, ω is the optical frequency, k_B is the Boltzmann constant, T is the temperature, and τ is the intra-band carrier relaxation time, assumed here to be 100 fs, as predicted for similar structures [42]. It is difficult to reach the anomalous regime in an

integrated high-speed device because the required electric fields (2.5 – 3.5 MV/cm) approach the typical breakdown fields of thin-film oxides. To date, this regime of high index change and low absorption has only been achieved by using ion/electrolyte gel gating [43] which is a fundamentally slow process. The low breakdown strength of many dielectrics has limited the state-of-the-art integrated graphene devices to modulating only the n_I of graphene [44,45].

3.1.3 Fabrication of Ionic-liquid gated SiN-TMD Platform

We lithographically defined 1.3-μm wide waveguides on 330-nm tall SiN with was deposited using LPCVD at 800 °C and annealed at 1200 °C for 3 hours on a 4-μm thermally oxidized SiO_2 layer with a combination of electron-beam lithorgraphy (EBL) (to define the waveguides) and deep ultraviolet (DUV) lithography (to pattern the CMP marks). We etched the SiN waveguides and CMP patterns using inductively coupled plasma-reactive ion etching (ICP-RIE) with a CHF_3/O_2 chemistry via an Oxford 100, followed by deposition of 600 nm of PECVD SiO_2 on the waveguides. We planarized the SiO_2 to ~100 nm above the SiN waveguides using standard CMP techniques to create a planar surface for the transfer of the MOCVD WS_2 monolayer and to prevent the TMD film from breaking at the waveguide edges. The power splitter (combiner) at the input (output) of the MZI structure was designed using a 1 × 2 (2 × 1) multimode interferometer (MMI). Due to the disproportionate ratio of the height (330 nm) to the width (1.3 μm) of the waveguide, and the sensitivity of the MMI structure, the MZI supports wavelength fringes from 1520 to 1630 nm for the TE mode and from 1455 to 1480 nm for the TM mode. A 10-nm layer of sacrificial thermal atomic layer-deposited (ALD) alumina was deposited on top of the SiO_2 to isolate the SiN waveguides from the subsequent fabrication steps required for the patterning the monolayer TMDs. Following the TMD preparation and the transfer and patterning described above, the metal contacts were lithographically patterned using a DUV mask aligner. In this work, 50/80 nm of Ti/Au was deposited by electron-beam evaporation followed by liftoff in acetone.

3.1.4 Fabrication of Capacitively Gated SiN-TMD Platform

We lithographically defined 1-μm wide waveguides on 360-nm tall SiN deposited using LPCVD at 800 ^oC and annealed at 1200 ^oC for 3 hours on 4-μm thermally oxidized SiO_2 using 248-nm deep ultraviolet lithography. We etch the SiN waveguides using the Oxford 100 ICP-RIE with a CHF_3/O_2 chemistry followed by the deposition of 600 nm of PECVD silicon dioxide (SiO_2) on the waveguides. We planarized the SiO_2 to about 260 nm {40 nm} above the SiN waveguides using standard CMP techniques to create a planar surface for the transfer of the WS_2 {MoS_2} monolayer and to prevent the TMD film from breaking at the waveguide edges. The 260 {40 nm} nm SiO_2 layer prevents the lossy ITO layer of the capacitor from interacting with the optical mode too strongly. Following this 45 nm {5 nm} of thermal ALD alumina is deposited on top of the SiO2 to isolate the waveguides from the subsequent fabrication steps for the TMD-HfO2-ITO capacitor. CVD is used to grow the monolayer and multilayer TMD on separate SiO2/Si substrates. We coat the TMD monolayer using 500-nm thick Poly(methyl methacrylate) (PMMA, A4, Chem), followed by baking the substrate at 180 ˚C for 5 min. The PMMA/TMD stack was delaminated from the SiO2/Si substrate by floating in a hot 1 M KOH solution with the PMMA side up. The PMMA/TMD stack is then rinsed in water a couple of times, before transferring it onto the SiN waveguides. After the transfer, the TMD clad waveguides are left to dry for a few hours before the PMMA was removed by soaking in acetone and rinsing in isopropanol. The transferred TMD is then patterned with a hydrogen silsesquioxane (HSQ)/PMMA stack using EBL, followed by

oxygen plasma and CHF_3/O_2 for etching residual PMMA and TMD. Metal contacts are then patterned on the TMD layer using EBL and 30 nm Ti/ 50 nm Au is deposited using electron-beam evaporation followed by a lift-off in acetone. 26 nm {37 nm} of thermal ALD Hafnia oxide at 200 °C is then deposited to form the dielectric for the TMD-HfO_2-ITO capacitor. The other electrode of the capacitor is first patterned using EBL and then ITO is sputtered at room temperature (24 °C), at a chamber base pressure of 12 mTorr with an argon flow of 30 sccm and an oxygen flow of 5 sccm followed by lift-off in acetone. To reduce the resistivity of the sputtered ITO film, the substrate is heated to a temperature of 200 °C and annealed in vacuum with the chamber pressure of 10 to 6 Torr, and an oxygen flow of 5 sccm for 30 minutes. Finally, the metal contacts to the ITO layer are patterned using EBL and 30 nm Ti and 50 nm Au is deposited using e-beam evaporation, followed by lift-off in acetone. To define devices with SU-8 on the composite SiN-WS_2 waveguides, SU-8 is photolithographically patterned on the waveguide and developed by spinning SU-8 to a thickness of 3.5 µm.

Note. The numbers in curly brackets {} indicate the dimensions for the composite SiN-MoS_2 devices.

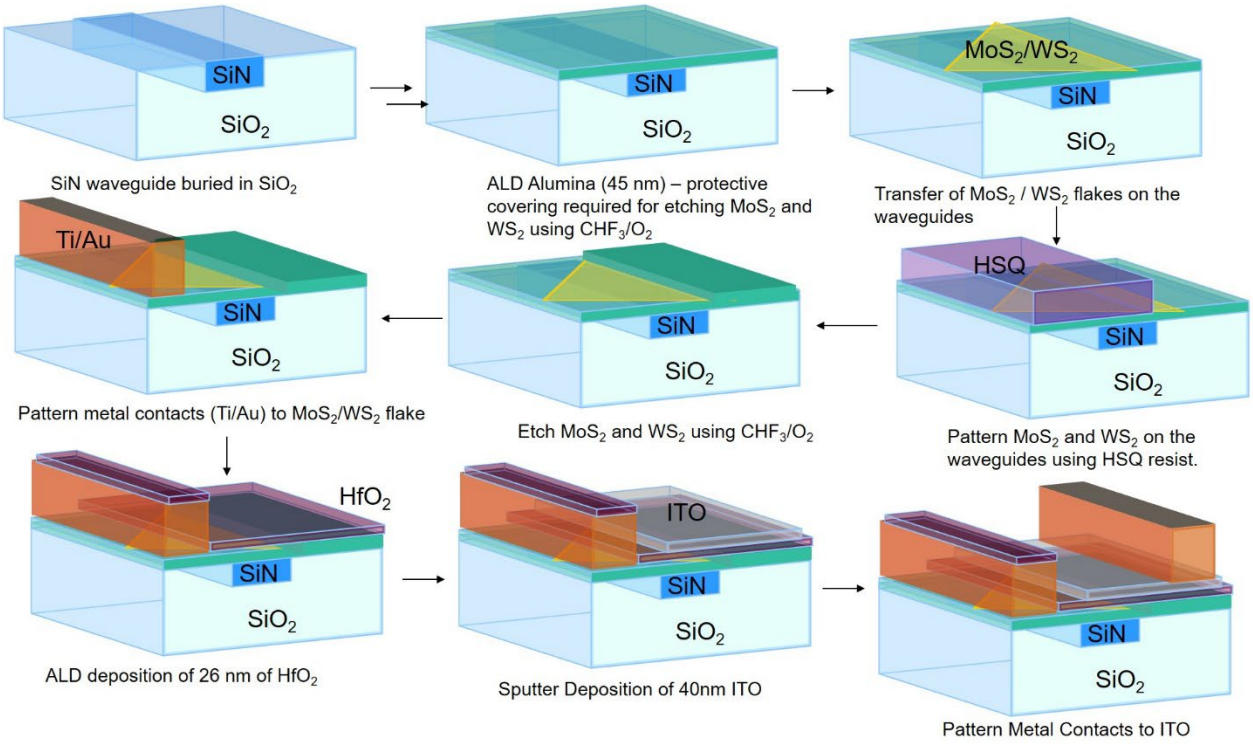

Figure 6: Fabrication Flow for SiN-TMD Capacitive Devices

3.1.5 Experimental setup

We coupled TE/TM polarized light from a tunable NIR laser (1450–1650 nm) into the SiN microring/MZI input using a tapered single-mode fiberwhile the optical output was collected at the SiN bus/MZI output using a similar tapered fiber. We recorded the microring/MZI

transmission spectrum for different bias voltages applied across the WS_2-HfO_2-ITO capacitor, to measure the phase shift and absorption change. We normalized each of the MZI/ring transmission spectra first by the maximum output power across the measured wavelength range and then by the optical power spectral profile measured at the output of one of the MZI arms by coupling light to a similar SiN waveguide with only one MMI splitter at the input of the MZI. The above normalization process eliminated the wavelength-dependent optical loss experienced by the incident laser light in the tapered optical fiber, the fiber polarizer, SiN waveguide and the MMI. This approach also accounts for the wavelength-dependent power fluctuations of the laser, if any. Note that these devices were all designed to operate optimally at 1550 nm with TE polarization.

Small-signal radiofrequency (RF) bandwidth measurements of the SiN-TMD low-loss phase shifters were made using a VNA in which we applied a DC bias voltage of 0 V across the WS_2-HfO_2-ITO capacitor combined with an RF signal of -10 dBm with a source impedance of 50 Ω (from the VNA).

3.1.6 Experimental Setup for Measuring Phase in Ring Resonators

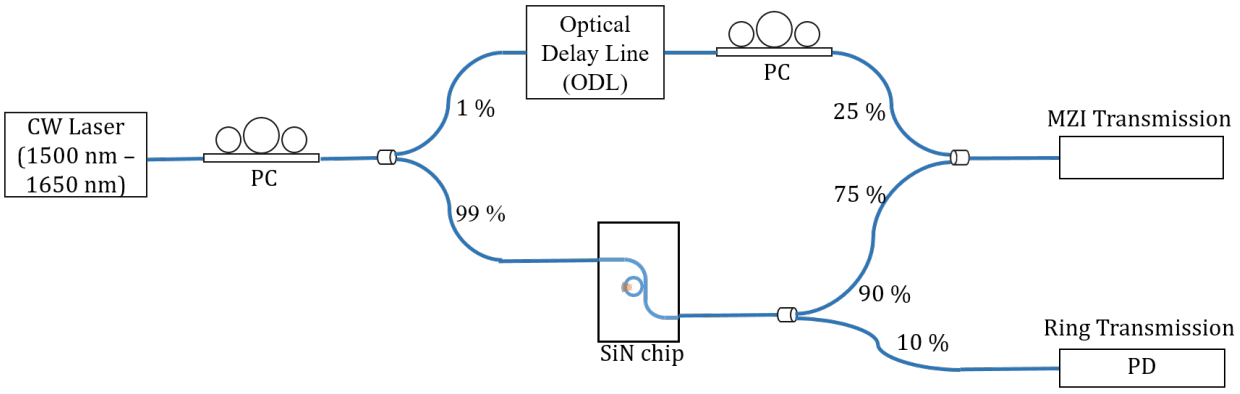

Figure 7: Experimental Setup to Measure Phase in Ring Assisted TMD-Graphene Phase Modulator

Figure 8: External Measurement Setup with Fibers Require Extensive Packing Material to Ensure Temperature/Air/Humidity Isolation for Phase Measurement in Ring Resonators

We measure the phase of a ring resonator as a function of wavelength by embedding the ring in an external fiber MZI and measuring both the ring and MZI transmission. Figure 7 shows the schematic of the experimental setup, where the light from the continuous wave (CW) laser source is first passed through a polarization controller (PC) to optimize the measurement by alighining the light for the TE mode and then to a 99:1 power splitter that divides the incoming light into the reference arm and the chip arm. We use a 99:1 power splitter to account for the 20-dB coupling loss from the input of the lensed fiber to the output of chip and finally to the output lensed fiber. A portion of the output from the chip (10%) is routed to a detector to measure the ring transmission (T_{Ring}), while 90% of the power is passed to the 75% arm of the output coupler. We embed a fiber-based optical delay line (ODL) to optimize the path length difference between the reference and the chip arm with a precision to a few 10's of μm. To optimize for the maximum extinction in the MZI fringes, we rotated the polarization of the light in the reference arm through a PC paddle, as seen in figure 7. Finally, we measure the response of the MZI using a photodetector at the output (T_{MZI}). Figure 8 shows a picture of the experimental setup implemented in the lab to measure the phase in a ring resonator. Fiber-based interferometers are quite susceptible to drifting due to changes in the local temperature, air flow, and humidity. One can minimize these drifts in the fiber MZIs by tapping the fibers down, covering free-space components (such as the PCs and ODL), and creating a box to house the entire setup.

4 RESULTS AND DISCUSSION

4.1 SiN-WS_2 low-loss MZI-based phase modulators

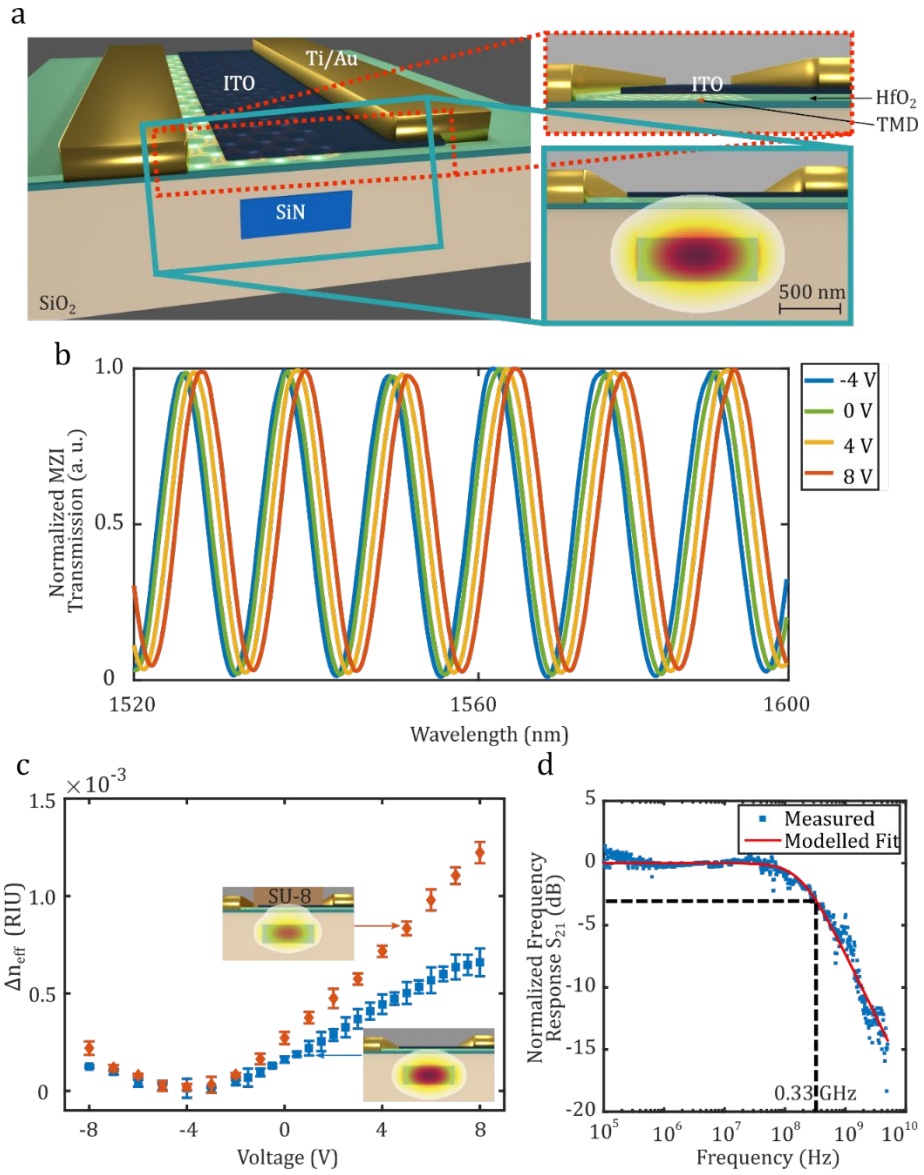

Figure 9: Capacitive SiN-TMD Platform for Low-loss, Low-power and High-speed Optical Phase Modulation

Illustration of the composite SiN-TMD waveguide, where the optical mode is shared between the SiN waveguide and the monolayer TMD. The inset details the TMD-HfO2-ITO parallel plate capacitor configuration which gates the monolayer WS2 by applying a bias voltage across the dielectric HfO2. (b) Normalized transmission response of MZI with different voltage applied across the capacitor on the longer arm of MZI. The right inset shows the optical micrograph of the fabricated phase modulator consisting of the composite waveguide in Fig. 2a embedded in the arms of an unbalanced MZI. (c) Change in the effective index measured from the MZI

spectra of the composite waveguide with and without SU-8 cladding. (d) Frequency response of the unclad SiN-WS_2 phase modulator measured at 1550 nm.

In our configuration quantum capacitance effects are negligible [9] and we estimate a linear induced charge density of $(0.37 \pm 0.05) \times 10^{12}$ cm^{-2} V^{-1}, based on the thickness (26 nm) and dielectric permittivity of the HfO_2. In contrast to the ionic liquid devices where the voltage swing is limited between −2 and 2 V, the voltage swing in these capacitive devices is determined by the thickness of the dielectric (HfO_2) and is in the range of −8 to 9 V. These MZIs are designed with a length imbalance of 100 μm between the two arms such that the transmission spectra exhibit clear fringes as the input laser wavelength is tuned from 1520 to 1620 nm when the TE mode is excited. In this device a 500-μm long WS_2-HfO_2-ITO capacitor is fabricated on each arm of the MZI. This is accomplished by starting with the transfer of chemical vapor deposition (CVD)-grown WS_2, followed by the deposition of HfO_2 and ITO, and subsequent patterning of metal electrodes (see Section 2.4). From the thickness of the HfO_2 (26 nm), we estimate an induced charge of $0.37 \pm 0.05 \times 10^{12}$ / cm^2 per volt applied to the gate.

Figure 9b shows the interference pattern at the MZI output for different voltages applied across the WS_2-HfO_2-ITO capacitor on the longer arm of the MZI. As in the ionic liquid gated devices, we induce a strong change in phase with applied voltage, thereby demonstrating a phase modulator with a modulation efficiency ($V_\pi L$) of 1.33 V·cm coupled with minimal change in extinction. Figure 9c shows the gating-induced Δn_{eff} of the composite waveguide, extracted by measuring the wavelength shift of the MZI spectra, which reaches 7×10^{-4} RIU for a swing voltage of 8 V. From the extremum point at −4 V in figure 9c, we infer that the charge neutrality point for the monolayer WS_2 layer occurs at −4 V which corresponds to an initial electron doping of $(1.5 \pm 0.2) \times 10^{12}$ cm^{-2}. This initial doping is probably due to sulfur vacancies arising from CVD growth, but can also arise from substrate effects or absorbents introduced in the transfer process [46].

Since the degree of phase change depends on the optical mode overlap with the monolayer WS_2, one can tailor the geometry of the waveguiding structures to engineer the mode overlap and take advantage of the full potential of this high change in index. As a proof of concept, we show here a decrease in $V_\pi L$, from 1.33 V·cm to 0.8 V·cm by enhancing the mode overlap with the monolayer WS_2 using SU-8 photoresist as a high-index (n=1.57) cladding material, as shown in inset of figure 9c. We estimate that the mode overlap for the unclad device is 0.016% while the mode overlap for the SU-8 clad device is 0.03%, based on our simulations (see Section 2.3). We show the experimentally measured Δn_{eff} for the unclad and SU-8 clad composite SiN-WS_2 waveguide in figure 9c. One can see that Δn_{eff} for the SU-8 clad device is 1.9 times the Δn_{eff} extracted for an unclad device, in agreement with the improvement in the mode overlap from our COMSOL simulations. The maximum measured Δn_{eff} for the SU-8 clad device is 1.35×10^{-3} RIU, which corresponds to a $V_\pi L$ of 0.8 V·cm.

We measured a 3-dB bandwidth of 0.3 GHz in our devices with a minimal DC electrical power dissipation of 0.64 nW in the WS_2-HfO_2-ITO capacitor (Figure 9d). The frequency response of the phase modulator was measured using a 40-GHz fast photodiode and an electrical vector network analyzer (VNA) at 1550 nm. The bandwidth is currently limited by the resistance of the

monolayer WS_2 and can be increased with improved electrical contacts, an optimized geometry, and better control over the initial doping density.

4.1.1 SiN-MoS_2 Low-Loss MZI-Based Phase Modulators

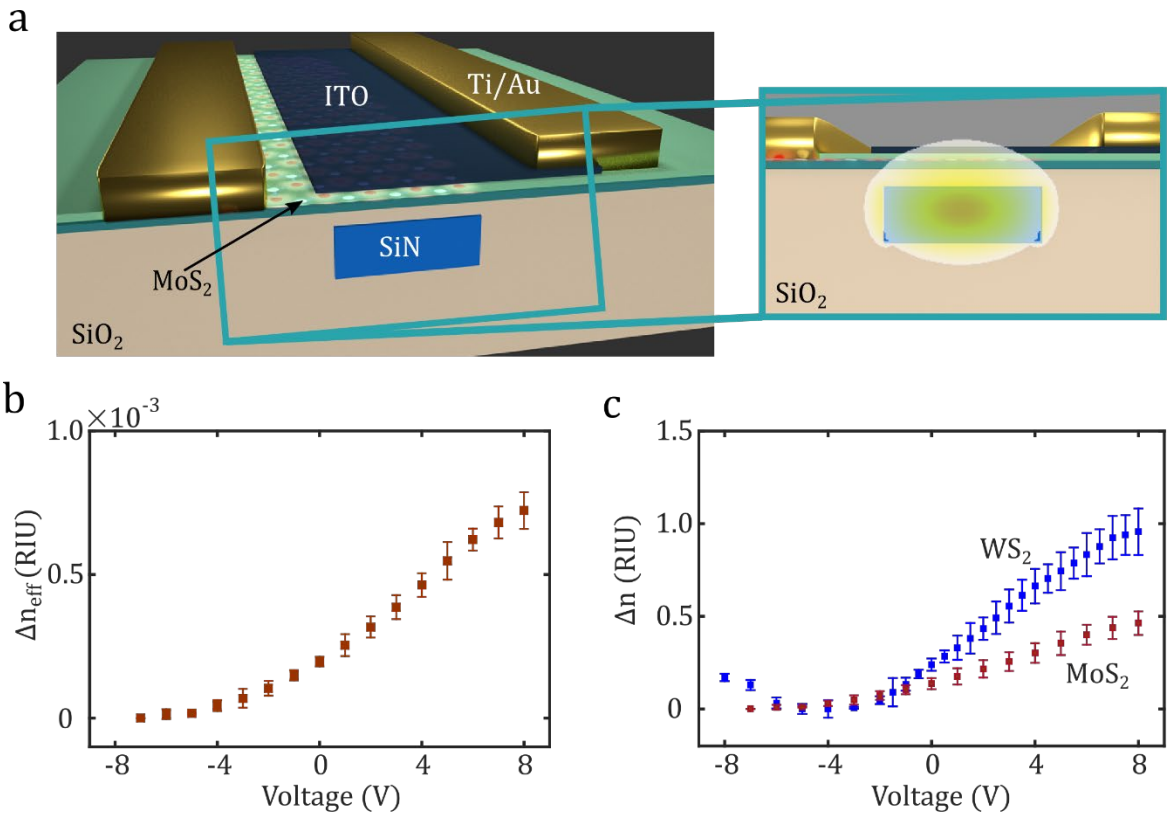

Figure 10: Phase Tuning of Monolayer MoS_2 in a Composite SiN-MoS_2 Waveguide
(a) Illustration of the composite SiN-MoS_2 waveguide, where the optical mode is shared between the SiN waveguide and monolayer MoS_2. The inset shows the optical mode profile for the composite SiN-MoS_2 waveguide, with an optical mode overlap of 0.054% with the monolayer MoS_2. (b) Change in the effective index ($|\Delta n_{eff}|$) of the propagating mode with voltage, extracted from the normalized MZI transmission spectra of the composite SiN-MoS_2 waveguide. (c) Extracted change in the refractive index of the monolayer TMDs, such as WS_2 and MoS_2, with a voltage swing of 8 V across the TMD-HfO_2-ITO capacitor.

4.1.2 Criticality of monolayer nature of TMD for electro-refractive response

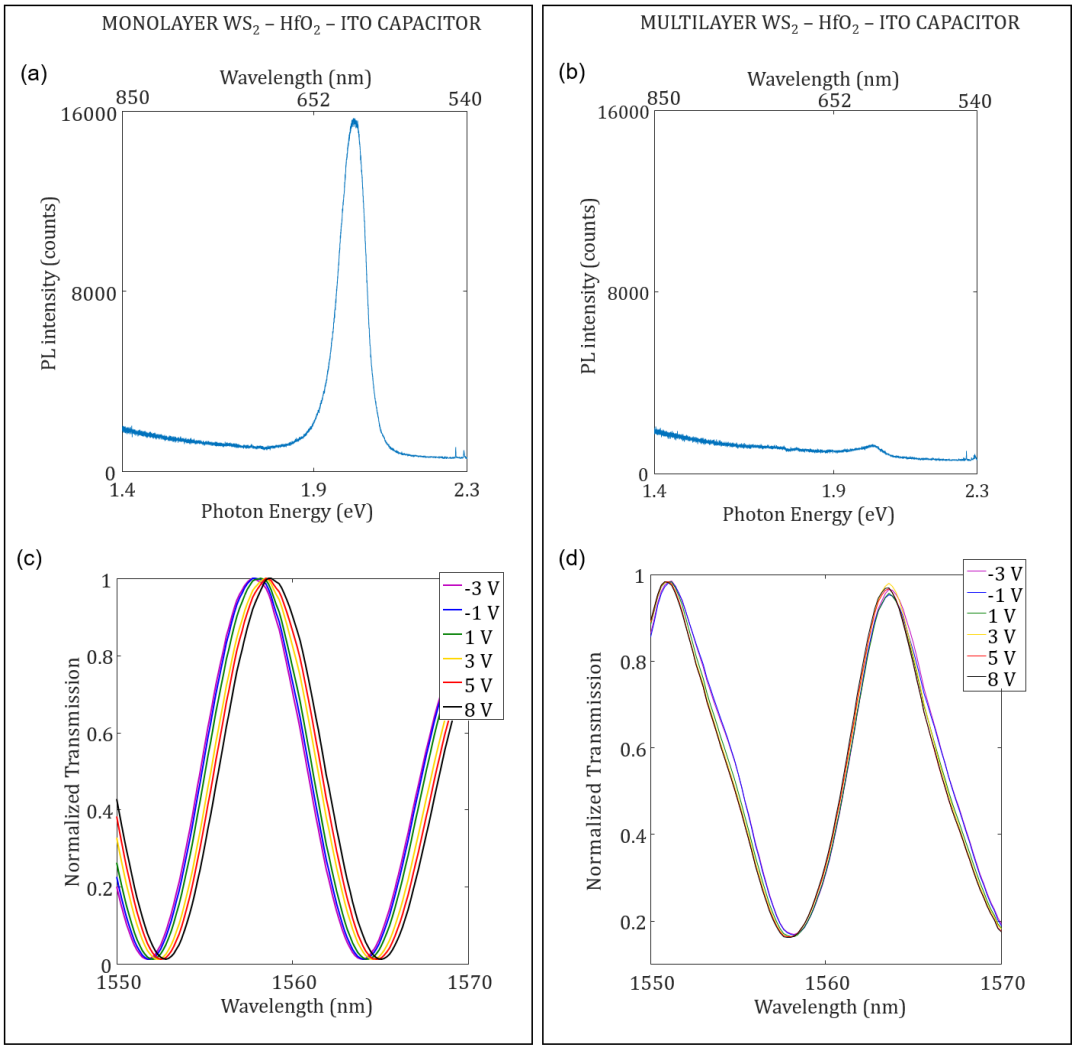

Figure 11: Criticality of the monolayer nature in strong electro-refractive response — A preliminary investigation.

As a preliminary investigation into the criticality of the monolayer nature of TMDs in observing the strong electro-refractive effect, we compare the performance of identical SiN MZI devices based on monolayer and multilayer WS_2 capacitors fabricated on the same wafer. As expected, the monolayer WS_2 film shows higher photoluminescence (PL) intensity (figure 11a) compared to a weak PL intensity for the multilayer WS_2 [47] (figure 11b). We observe a strong gating-induced phase shift in the MZI transmission spectra for monolayer WS_2-based devices (figure 11c), compared to a negligible phase shift in the multilayer WS_2-based devices (figure 11d). The MZI devices used for this comparison are identical to the ones shown in figure 4 but with a 200-µm long capacitor on each arm. Note: The MZI used for calibrating the phase modulation efficiency of the devices based on multilayer WS_2 is designed to be unbalanced in power with 33:67 power splitting ratio in the shorter/longer arm of the MZI using a directional coupler at the

input of the MZI and a 50:50 MMI at the output of MZI. This causes the non-zero extinction in the MZI transmission spectrum in figure 11b.

The absence of a strong electro-refractive change in multilayer TMD films could be due to the comparatively weaker exctionic contribution to the index of refraction. The phase change is expected to be especially strong in direct bandgap 2D materials compared to their bulk counterparts because the weak dielectric screening of monolayer TMDs result in enhanced Coulombic interactions and strong exciton binding energy [10,48]. This section discusses specific results.

4.1.3 Performance of ring-based TMD-graphene composite low-loss phase modulator

Figure 12a explors the strong change in coupling between the bus waveguide and ring resonator from the under-coupled to the over-coupled regime by applying an electrostatic field across the 25-μm long WSe_2-Al_2O_3-graphene capacitor embedded in the ring resonator configuration. Initially (at 0 V), the ring is in the under-coupled state, where the light propagating in the bus waveguide is weakly coupled to the lossy ring resonator. As the applied voltage is increased, the loss in the graphene reduces. This leads to an increase in the coupling between the waveguide and ring resonator, thereby transitioning it from the under-coupled regime (at 0 V) to the critically coupled regime (at 8.5 V) and subsequently to the over-coupled regime (beyond 12 V). This transition between coupling regimes is highlighted in the transmission spectrum provided in the bottom panel of figure 12a. One can track the evolution of the extracted phase spectra with voltage in the top panel of figure 12a, obtained by theoretically fitting the measured transmission spectra with the ring resonator equation [49].

Theoretical fitting (see figure 12b) indicates that our 25-μm long device can induce a phase change of $\pi/2$ with a voltage swing from 10 to 30 V at a probe wavelength of 1646.19 nm with an amplitude modulation of 2 dB and a low insertion loss of 3 dB. We further show, in figure 12c, that this modulator is also capable of performing digital phase shift keying by inducing an optical phase shift of π radians while transitioning between the under-coupled (8 V) and over-coupled regime (30 V) with insignificant amplitude modulation and an insertion loss of 5 dB. The electro-optic bandwidth of the 25-μm WSe_2-graphene device is RC limited to a 3-dB operating frequency of 15 GHz. We can further improve the operating bandwidth of the device by engineering the metal-TMD and metal-graphene contacts.

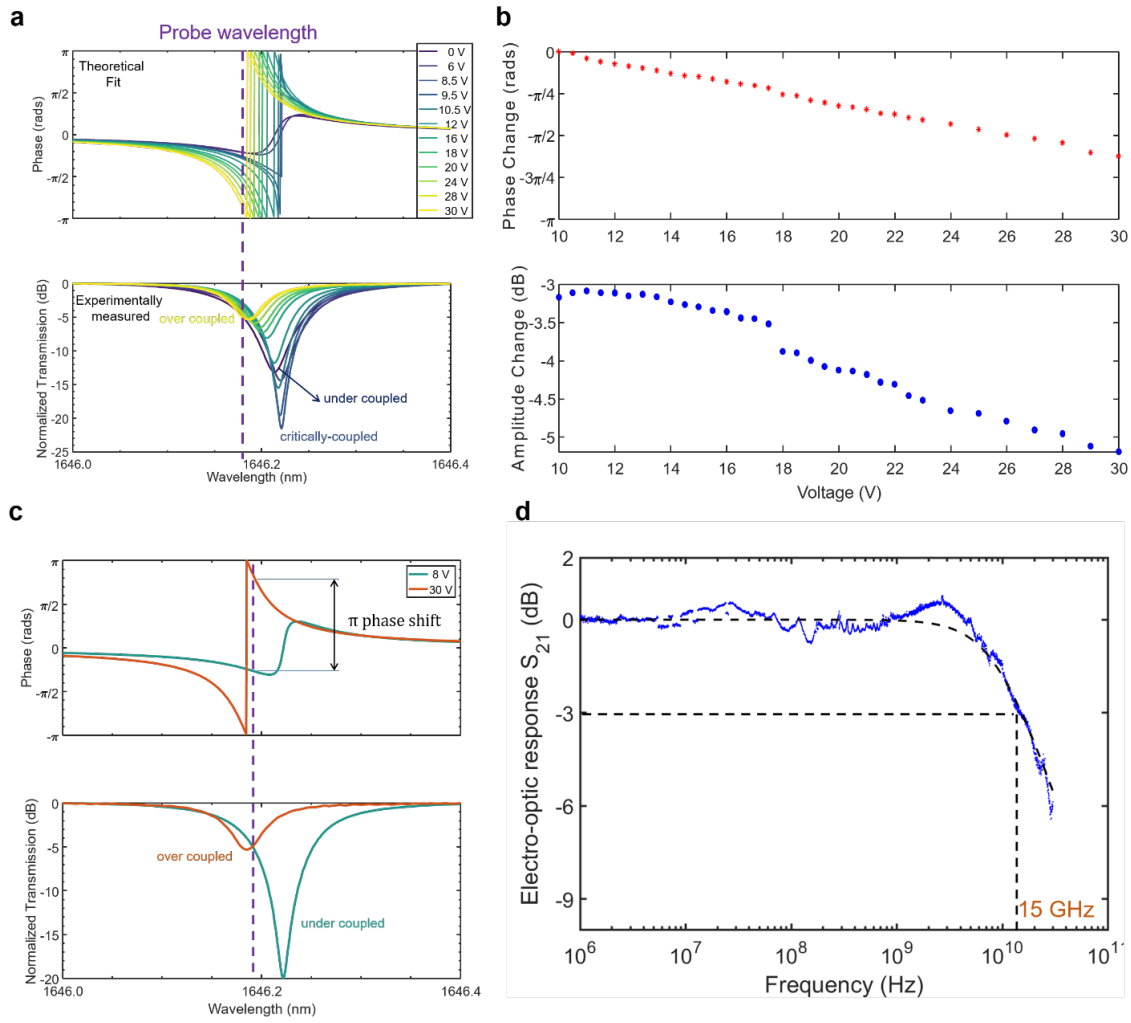

Figure 12: Experimentally Measured Optical Transmission and Electro-optic Bandwidth of WSe_2-graphene Based Composite Waveguide

(a) Experimentally measured normalized transmission (bottom panel) and theoretical fit phase spectra (top panel) of a bus coupled microring resonator with 25-μm long WSe_2-Al2O3-graphene capacitor for different voltages applied across graphene and WSe_2 electrode. The strong change in coupling can be attributed to the strongly tunable absorption in monolayer graphene, while the shift in resonance wavelength is dependent on a combination of the electro-refractive effect in both graphene and monolayer WSe_2. (b) Extracted phase change of π/2 radians with an amplitude modulation of ~ 2 dB and an insertion loss of 3 dB at a probe wavelength of 1646.18 nm (dashed blue line in figure 2a) for a voltage swing from 10 to 30 V. (c) One can leverage the same device to achieve a digital π phase shift at a probe wavelength of 1646.19 nm with insignificant amplitude modulation and an insertion loss of 5 dB by tuning between the under-coupled regime (at 8 V) and the over-coupled regime (at 30 V). (d) Normalized frequency response (S21) of the WSe_2-graphene-based SiN phase modulator at a wavelength of 1646.2 nm (blue squares) shows a 3-dB electro-optic bandwidth of 14.9 ± 0.1 GHz.

We show the change in propagation loss (dB/μm) and effective index of the hybrid mode as a function of the applied voltage in figure 13a by extracting and fitting the experimentally measured transmission (figure 2a) to the theoretically simulated ring resonator equation using MATLAB. One can see that the propagation loss in the WSe_2–SiN mode reduces from 0.025 dB/μm at 0 V (initial doping density of 5.5×10^{12} cm^{-2}) to 0.00026 dB/μm at 30 V (final doping density of 3.16×10^{13} cm^{-2}). At the same time the effective index initially undergoes a red shift of 1.2×10^{-4} (refractive index units (RIU)) from 0 to 8 V followed by a strong blue shift reaching a maximum index change of 5.6×10^{-4} (RIU) from 8 to 30 V. We attribute the change in propagation loss with voltage to the reduction in absorption of the monolayer graphene with doping as a signature of Pauli blocking that appears at doping densities above 2×10^{13} cm^{-2} (∼17 V) where graphene becomes transparent. Meanwhile, the change in effective index is influenced by both the monolayer graphene and monolayer WSe_2, with the electro-refractive response of graphene being dominant at low doping densities [$< 1.4\times10^{13}$ cm^{-2} (at 10 V)] and the strong blue-detuned electro-refractive response of WSe_2 being the influencing factor for index change at high doping densities ($> 1.4\times10^{13}$ cm^{-2}).

4.1.3.1 Extracting the electro-optic response of monolayer graphene and TMD

We design compact and efficient phase modulators by leveraging the observed electro-absorptive property of graphene that is dominant at low doping densities (see the real part of the extracted graphene conductivity in figure 13b, which contributes to absorption) and the strong electro-refractive response in monolayer WSe_2 (see figure 13c) which is the dominant mechanism at high doping densities. At operating voltages below 10 V (i.e. in the low doping regime) the absorption of graphene is modulated strongly which causes the coupling condition between the bus waveguide and ring resonator to change from the under-coupled to the critically coupled regime. In the latter case, the phase profile at the output of ring resonator is marginally dispersive (see top panel of figure 12a). Beyond 10 V the resonator enters the over-coupled regime, where the phase profile is highly dispersive and the resonance wavelength of the ring resonator is blue detuned with applied voltage and dominated by the electro-refractive property of WSe_2. Here, the blue detuning causes a shift in the transmission and phase spectra and the loss modulation in graphene modifies the linewidth and extinction, thereby rendering a regime of operation where the phase is strongly modulated with minimal amplitude modulation with low insertion loss at a probe wavelength of 1646.19 nm. From our COMSOL modelling, we predict a change of about 18% in the refractive index of monolayer WSe_2 with a doping density of 3.1×10^{13} cm^{-2} at 30 V and find, at these doping densities, that the monolayer graphene has been doped to the transparency regime (see figure 13c and figure 13b, respectively). When compared to traditional bulk electro-refractive materials such as silicon, where the change in index is only a fraction of the index, monolayer TMDs exhibit a strong electro-refractive response.

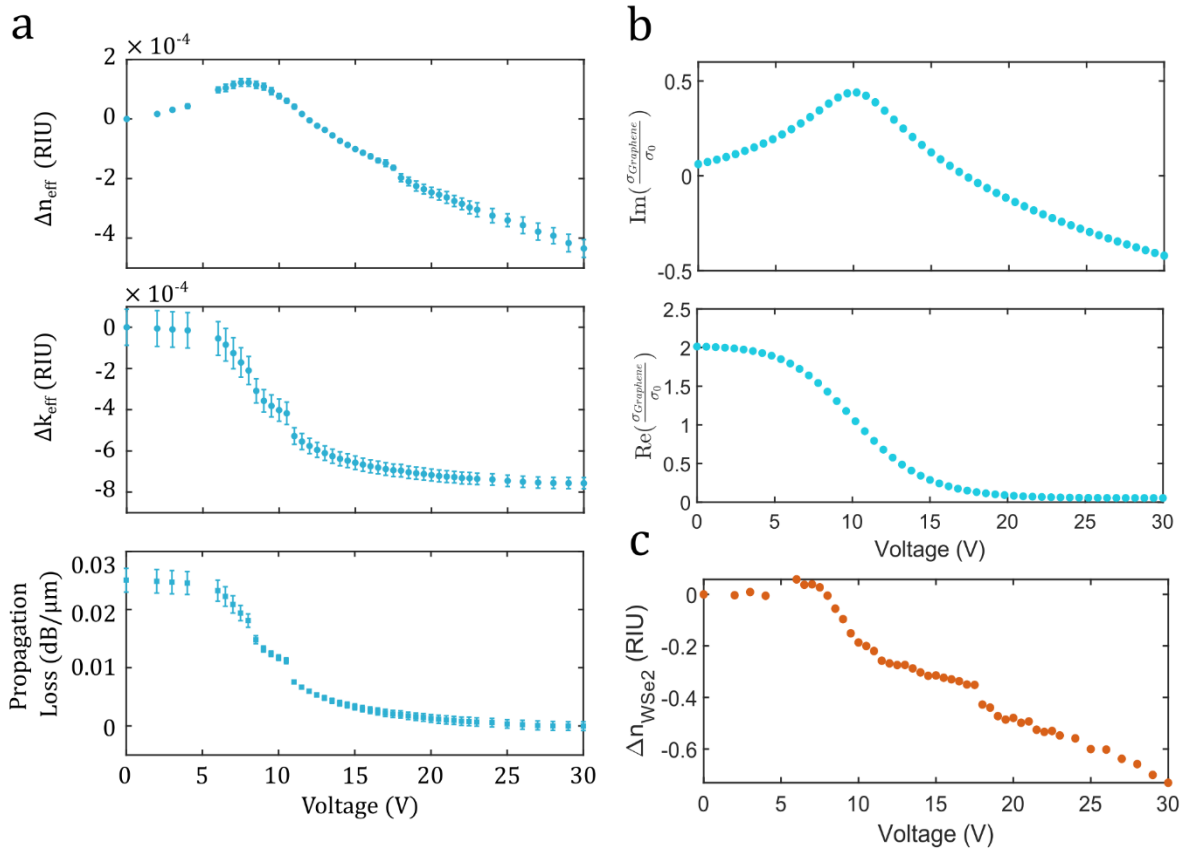

Figure 13: Theoretically Computed Real and Imaginary Part of the Index of Propagating Mode, Monolayer Graphene and Monolayer WSe_2.

(a) a) Change in the real (top panel) and imaginary (middle panel) part of the effective index (Δn_{eff} and Δk_{eff}) of the hybrid WSe_2-graphene SiN waveguide at different voltages extracted from the normalized transmission measured in the bottom panel of figure 8a. The bottom panel of the figure shows the change in propagation loss (dB/μm) of the propagating mode with various voltages applied across the WSe_2-Al_2O_3-graphene capacitor. The error bars account for the root mean square (rms) error from the numerical fit and a ± 2 μm error in the patterned length of the monolayers. (b) Change in the imaginary and real part of the normalized complex conductivity of graphene (σ_Graphene/σ_0) with voltage, extracted from the change in effective index in (a) using COMSOL simulations. The Im{σ_Graphene/σ_0} (top panel) is related to the real part of the dielectric permittivity, which contributes to the change in real part of index of the propagating mode, whereas the Re{σ_Graphene/σ_0} (bottom panel) contributes to the imaginary part of dielectric permittivity and hence absorption. One can see that the bottom panel of (b) closely tracks the change in propagation loss [bottom panel in (a)], which suggests that the graphene becomes transparent with applied voltage due to Pauli blocking at high doping densities. (c) Change in the real part of refractive index of monolayer WSe_2 with applied voltage, extracted from the effective index change in (a). One can see that the index of monolayer WSe_2 changes by almost 18%.

4.1.3.2 Measured Phase in ring assisted compact phase modulators

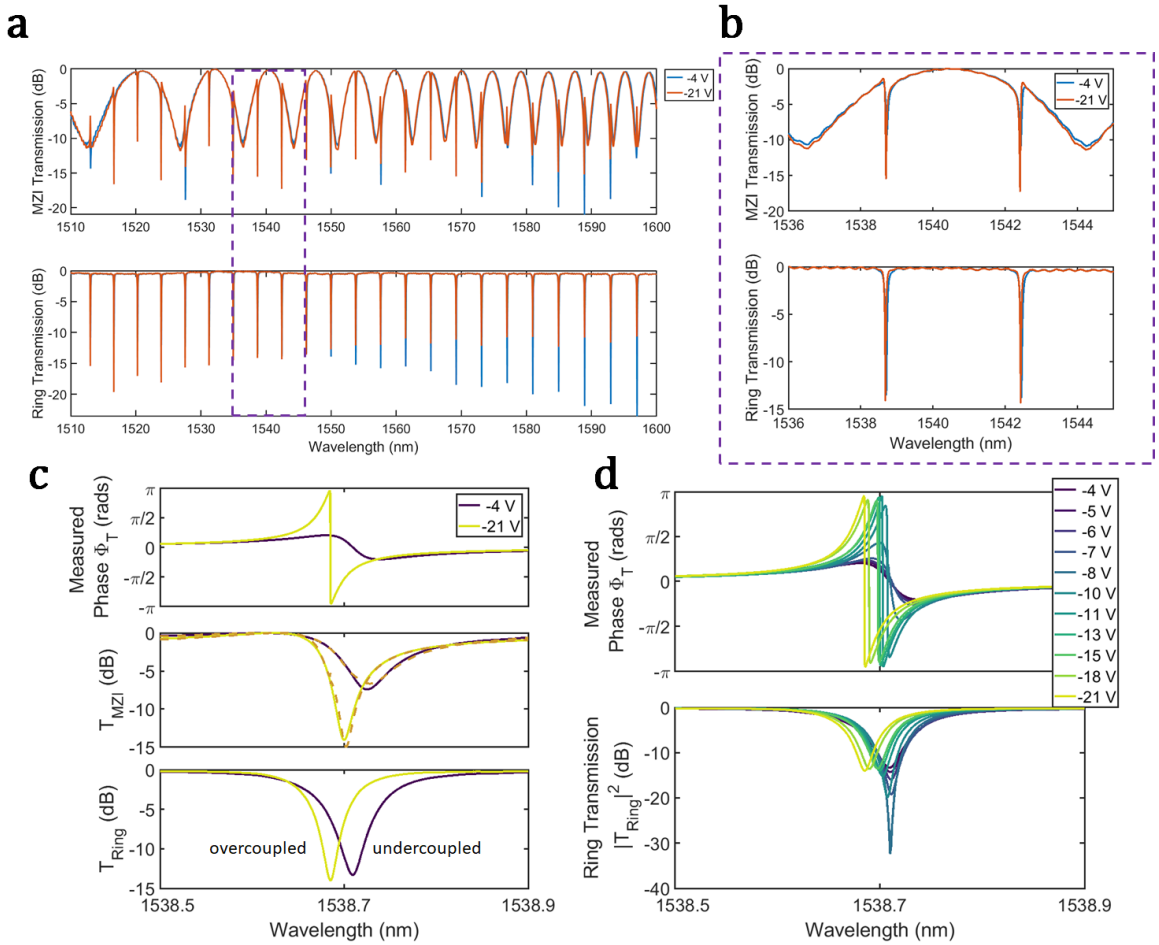

Figure 14: Measured phase of a ring based 40-µm long WSe_2-graphene hybrid waveguide in an external fiber MZI

(a) Top panel of the figure shows the measured spectrum of the normalized MZI transmission as a function of wavelength for {-4 and -21 V}, which depicts the under-coupled and over-coupled regime of the ring resonator operation. The fringes at -4 and -21 V overlap each other signifying that the fiber MZI is stable, whereas the phase near the resonance is modified. The bottom panel shows the normalized measured ring transmission as a function of wavelength for -4 V and -21 V. (b) Normalized MZI and ring transmission for the wavelength range of 1536 to 1545 nm. We use the MZI fringes to extract an optical path length of ~ 200 µm between the reference and chip arm. (c) Measured phase ϕ_T, normalized MZI transmission (T_{MZI}), and normalized ring transmission (T_{Ring}) as a function of wavelength from 1538.5 to 1538.9 nm with the voltages of -4 V when the ring is in the under-coupled regime and at -21 V when the ring is over coupled. At 1538.7 nm the ring transmission barely changes with an insertion loss of -9 dB, however the phase drastically changes by 0.82 π causing a strong change in the MZI extinction (middle panel). (d) Measured phase (ϕT) and normalized ring transmission for different voltages shows the evolution of the phase spectrum as the ring resonator transitions from the under-coupled regime (at -4 V) to the critically coupled regime (at -8 V) and finally to the over-coupled regime (at -21 V).

5 CONCLUSIONS

In this work, we are the first to observe strong electro-refractive effects in semiconductor transition metal dichalcogenides (TMDs) in the near-infrared range (far below the excitonic resonance), where the TMDs are transparent [36]. We use this strong effect to demonstrate photonic devices based on a composite SiN-TMD platform that can achieve significant phase modulation with minimal induced loss and low electrical power consumption.

We measure a strong doping-induced change in the refractive index (Δn) of 0.53 in WS_2 with minimal induced absorption (Δk) of 0.004. This $|\Delta n/\Delta k|$ of ~125, is an order of magnitude higher than the previously measured $|\Delta n/\Delta k|$ for various 2D monolayers or for bulk materials commonly employed in silicon photonics, such as silicon (see Figure 1d).

We utilize this strong electro-optic response to demonstrate ultra-low power, lossless, optical phase modulation based on a composite SiN-TMD platform. The WS_2-based photonic modulator achieves efficiency ($V_\pi L$) of 0.8 V·cm, an RC limited bandwidth of 0.3 GHz, and a DC electrical power consumption of 0.64 nW. A similarly strong electro-refractive effect was also observed in monolayer MoS_2. The measured index change (~15%) in these TMDs is unprecedented, considering that the change in index of bulk $LiNbO_3$ – the 'gold standard' for photonics is typically 0.04%.

We rely on the strong electro-refractive response in TMDs (WSe_2) [50] and strongly tunable absorption in graphene [51] to demonstrate an ultra-compact phase shifter (only 25-μm long), which consists of a WSe_2 – alumina (Al_2O_3)-graphene capacitor placed atop an optical microring resonator. We further report that our devices support an electro-optic bandwidth of 15 GHz (~ 50 times higher than the electro-optic bandwidth reported on a TMD platform to date).

6 RECOMMENDATIONS

Future work:

- In our first generation devices we leveraged ITO as our transparent conducting electrode, however the insertion loss due to a 500-μm long ITO electrode with 40-nm thickness is 6 dB. This insertion loss can be reduced by replacing the ITO with another conducting electrode such as doped graphene. We have worked on this in the past and showed in Ref. [52], that p-doped graphene can act as the low-loss electrode with 2 orders of magnitude lower loss than ITO.
- We believe that we can further improve the bandwidth performance of these devices by engineering graphene edge contacts.
- We can develop efficient, low-loss switches in large-scale photonic structures using our ultra-compact, high-speed and low-loss phase modulators.

7 REFERENCES

1. K. F. Mak and J. Shan, "Photonics and optoelectronics of 2D semiconductor transition metal dichalcogenides," Nature Photonics **10**, 216–226 (2016).
2. F. Bonaccorso, Z. Sun, T. Hasan, and A. C. Ferrari, "Graphene photonics and optoelectronics," Nature Photonics **4**, 611–622 (2010).
3. F. Xia, H. Wang, D. Xiao, M. Dubey, and A. Ramasubramaniam, "Two-dimensional material nanophotonics," Nature Photonics **8**, 899–907 (2014).
4. S. Manzeli, D. Ovchinnikov, D. Pasquier, O. V. Yazyev, and A. Kis, "2D transition metal dichalcogenides," Nature Reviews Materials **2**, 17033 (2017).
5. J. S. Ross, S. Wu, H. Yu, N. J. Ghimire, A. M. Jones, G. Aivazian, J. Yan, D. G. Mandrus, D. Xiao, W. Yao, and X. Xu, "Electrical control of neutral and charged excitons in a monolayer semiconductor," Nature Communications **4**, 1474 (2013).
6. A. Chernikov, A. M. van der Zande, H. M. Hill, A. F. Rigosi, A. Velauthapillai, J. Hone, and T. F. Heinz, "Electrical Tuning of Exciton Binding Energies in Monolayer WS_2," Phys. Rev. Lett. **115**, 126802 (2015).
7. G. Wang, A. Chernikov, M. M. Glazov, T. F. Heinz, X. Marie, T. Amand, and B. Urbaszek, "Colloquium: Excitons in atomically thin transition metal dichalcogenides," Rev. Mod. Phys. **90**, 021001 (2018).
8. Y. Yu, Y. Yu, L. Huang, H. Peng, L. Xiong, and L. Cao, "Giant Gating Tunability of Optical Refractive Index in Transition Metal Dichalcogenide Monolayers," Nano Lett. **17**, 3613–3618 (2017).
9. D. Braga, I. Gutiérrez Lezama, H. Berger, and A. F. Morpurgo, "Quantitative Determination of the Band Gap of WS_2 with Ambipolar Ionic Liquid-Gated Transistors," Nano Lett. **12**, 5218–5223 (2012).
10. Y. Li, A. Chernikov, X. Zhang, A. Rigosi, H. M. Hill, A. M. van der Zande, D. A. Chenet, E.-M. Shih, J. Hone, and T. F. Heinz, "Measurement of the optical dielectric function of monolayer transition-metal dichalcogenides: MoS_2, $MoSe_2$, WS_2, and WSe_2," Phys. Rev. B **90**, 205422 (2014).
11. R. Soref and B. Bennett, "Electrooptical effects in silicon," IEEE Journal of Quantum Electronics **23**, 123–129 (1987).
12. Z. Jin, X. Li, J. T. Mullen, and K. W. Kim, "Intrinsic transport properties of electrons and holes in monolayer transition-metal dichalcogenides," Phys. Rev. B **90**, 045422 (2014).
13. F. A. Rasmussen and K. S. Thygesen, "Computational 2D Materials Database: Electronic Structure of Transition-Metal Dichalcogenides and Oxides," J. Phys. Chem. C **119**, 13169–13183 (2015).
14. A. Woessner, Y. Gao, I. Torre, M. B. Lundeberg, C. Tan, K. Watanabe, T. Taniguchi, R. Hillenbrand, J. Hone, M. Polini, and F. H. L. Koppens, "Electrical 2π phase control of infrared light in a 350-nm footprint using graphene plasmons," Nature Photonics **11**, 421–424 (2017).
15. M. Mohsin, D. Neumaier, D. Schall, M. Otto, C. Matheisen, A. L. Giesecke, A. A. Sagade, and H. Kurz, "Experimental verification of electro-refractive phase modulation in graphene," Scientific Reports **5**, 10967 (2015).
16. S. W. Ye, F. Yuan, X. H. Zou, M. K. Shah, R. G. Lu, and Y. Liu, "High-Speed Optical Phase Modulator Based on Graphene-Silicon Waveguide," IEEE Journal of Selected Topics in Quantum Electronics **23**, 1–5 (2017).

17. C. T. Phare, Y.-H. Daniel Lee, J. Cardenas, and M. Lipson, "Graphene electro-optic modulator with 30 GHz bandwidth," Nature Photonics **9**, 511–514 (2015).
18. K. F. Mak, K. He, C. Lee, G. H. Lee, J. Hone, T. F. Heinz, and J. Shan, "Tightly bound trions in monolayer MoS_2," Nature Materials **12**, 207–211 (2013).
19. S. Akiyama, T. Baba, M. Imai, T. Akagawa, M. Takahashi, N. Hirayama, H. Takahashi, Y. Noguchi, H. Okayama, T. Horikawa, and T. Usuki, "12.5-Gb/s operation with 0.29-V·cm $V_\pi L$ using silicon Mach–Zehnder modulator based-on forward-biased pin diode," Opt. Express, OE **20**, 2911–2923 (2012).
20. A. Liu, R. Jones, L. Liao, D. Samara-Rubio, D. Rubin, O. Cohen, R. Nicolaescu, and M. Paniccia, "A high-speed silicon optical modulator based on a metal–oxide–semiconductor capacitor," Nature **427**, 615–618 (2004).
21. D. Marris-Morini, L. Vivien, J. M. Fédéli, E. Cassan, P. Lyan, and S. Laval, "Low loss and high speed silicon optical modulator based on a lateral carrier depletion structure," Opt. Express, OE **16**, 334–339 (2008).
22. X. Xiao, H. Xu, X. Li, Z. Li, T. Chu, Y. Yu, and J. Yu, "High-speed, low-loss silicon Mach–Zehnder modulators with doping optimization," Opt. Express, OE **21**, 4116–4125 (2013).
23. J.-H. Han, F. Boeuf, J. Fujikata, S. Takahashi, S. Takagi, and M. Takenaka, "Efficient low-loss InGaAsP/Si hybrid MOS optical modulator," Nature Photonics **11**, 486–490 (2017).
24. Y.-C. Chang, C.-H. Liu, C.-H. Liu, Z. Zhong, and T. B. Norris, "Extracting the complex optical conductivity of mono- and bilayer graphene by ellipsometry," Applied Physics Letters **104**, 261909 (2014).
25. T. Stauber, N. M. R. Peres, and A. K. Geim, "Optical conductivity of graphene in the visible region of the spectrum," Phys. Rev. B **78**, 085432 (2008).
26. N. C. Harris, G. R. Steinbrecher, M. Prabhu, Y. Lahini, J. Mower, D. Bunandar, C. Chen, F. N. C. Wong, T. Baehr-Jones, M. Hochberg, S. Lloyd, and D. Englund, "Quantum transport simulations in a programmable nanophotonic processor," Nature Photonics **11**, 447–452 (2017).
27. Y. Shen, N. C. Harris, S. Skirlo, M. Prabhu, T. Baehr-Jones, M. Hochberg, X. Sun, S. Zhao, H. Larochelle, D. Englund, and M. Soljačić, "Deep learning with coherent nanophotonic circuits," Nature Photonics **11**, 441–446 (2017).
28. J. K. Doylend, M. J. R. Heck, J. T. Bovington, J. D. Peters, L. A. Coldren, and J. E. Bowers, "Two-dimensional free-space beam steering with an optical phased array on silicon-on-insulator," Opt. Express, OE **19**, 21595–21604 (2011).
29. J. Sun, E. Timurdogan, A. Yaacobi, E. S. Hosseini, and M. R. Watts, "Large-scale nanophotonic phased array," Nature **493**, 195–199 (2013).
30. S. A. Miller, S. A. Miller, C. T. Phare, C. T. Phare, Y.-C. Chang, Y.-C. Chang, X. Ji, X. Ji, O. A. J. Gordillo, O. A. J. Gordillo, A. Mohanty, A. Mohanty, S. P. Roberts, S. P. Roberts, M. C. Shin, M. C. Shin, B. Stern, B. Stern, M. Zadka, M. Zadka, and M. Lipson, "512-Element Actively Steered Silicon Phased Array for Low-Power LIDAR," in *Conference on Lasers and Electro-Optics (2018), Paper JTh5C.2* (Optical Society of America, 2018), p. JTh5C.2.
31. N. C. Harris, Y. Ma, J. Mower, T. Baehr-Jones, D. Englund, M. Hochberg, and C. Galland, "Efficient, compact and low loss thermo-optic phase shifter in silicon," Opt. Express, OE **22**, 10487–10493 (2014).

32. A. Masood, M. Pantouvaki, D. Goossens, G. Lepage, P. Verheyen, J. V. Campenhout, P. Absil, D. V. Thourhout, and W. Bogaerts, "Fabrication and characterization of CMOS-compatible integrated tungsten heaters for thermo-optic tuning in silicon photonics devices," Opt. Mater. Express, OME **4**, 1383–1388 (2014).
33. Y.-C. Chang, S. P. Roberts, B. Stern, and M. Lipson, "Resonance-Free Light Recycling," arXiv: 1710.02891 (2017).
34. E. Timurdogan, C. V. Poulton, M. J. Byrd, and M. R. Watts, "Electric field-induced second-order nonlinear optical effects in silicon waveguides," Nature Photonics **11**, 200–206 (2017).
35. C. Wang, M. Zhang, B. Stern, M. Lipson, and M. Lončar, "Nanophotonic lithium niobate electro-optic modulators," Opt. Express, OE **26**, 1547–1555 (2018).
36. I. Datta, S. H. Chae, G. R. Bhatt, M. A. Tadayon, B. Li, Y. Yu, C. Park, J. Park, L. Cao, D. N. Basov, J. Hone, and M. Lipson, "Low-loss composite photonic platform based on 2D semiconductor monolayers," Nature Photonics **14**, 256–262 (2020).
37. Q. Xu, B. Schmidt, S. Pradhan, and M. Lipson, "Micrometre-scale silicon electro-optic modulator," Nature **435**, 325–327 (2005).
38. A. Yariv, "Universal relations for coupling of optical power between microresonators and dielectric waveguides," Electronics Letters **36**, 321–322 (2000).
39. N. K. Emani, T.-F. Chung, A. V. Kildishev, V. M. Shalaev, Y. P. Chen, and A. Boltasseva, "Electrical Modulation of Fano Resonance in Plasmonic Nanostructures Using Graphene," Nano Lett. **14**, 78–82 (2014).
40. M. Lafkioti, B. Krauss, T. Lohmann, U. Zschieschang, H. Klauk, K. v. Klitzing, and J. H. Smet, "Graphene on a Hydrophobic Substrate: Doping Reduction and Hysteresis Suppression under Ambient Conditions," Nano Lett. **10**, 1149–1153 (2010).
41. J. W. Suk, W. H. Lee, J. Lee, H. Chou, R. D. Piner, Y. Hao, D. Akinwande, and R. S. Ruoff, "Enhancement of the Electrical Properties of Graphene Grown by Chemical Vapor Deposition via Controlling the Effects of Polymer Residue," Nano Lett. **13**, 1462–1467 (2013).
42. Y.-W. Tan, Y. Zhang, K. Bolotin, Y. Zhao, S. Adam, E. H. Hwang, S. Das Sarma, H. L. Stormer, and P. Kim, "Measurement of Scattering Rate and Minimum Conductivity in Graphene," Phys. Rev. Lett. **99**, 246803 (2007).
43. V. Sorianello, G. D. Angelis, T. Cassese, M. Midrio, M. Romagnoli, M. Mohsin, M. Otto, D. Neumaier, I. Asselberghs, J. V. Campenhout, and C. Huyghebaert, "Complex effective index in graphene-silicon waveguides," Opt. Express, OE **24**, 29984–29993 (2016).
44. C. T. Phare, Y.-H. Daniel Lee, J. Cardenas, and M. Lipson, "Graphene electro-optic modulator with 30 GHz bandwidth," Nature Photon **9**, 511–514 (2015).
45. M. Liu, X. Yin, E. Ulin-Avila, B. Geng, T. Zentgraf, L. Ju, F. Wang, and X. Zhang, "A graphene-based broadband optical modulator," Nature **474**, 64–67 (2011).
46. J. T. Mlack, P. Masih Das, G. Danda, Y.-C. Chou, C. H. Naylor, Z. Lin, N. P. López, T. Zhang, M. Terrones, A. T. C. Johnson, and M. Drndić, "Transfer of monolayer TMD WS_2 and Raman study of substrate effects," Scientific Reports **7**, 43037 (2017).
47. H. R. Gutiérrez, N. Perea-López, A. L. Elías, A. Berkdemir, B. Wang, R. Lv, F. López-Urías, V. H. Crespi, H. Terrones, and M. Terrones, "Extraordinary Room-Temperature Photoluminescence in Triangular WS2 Monolayers," Nano Lett. **13**, 3447–3454 (2013).

48. T. Mueller and E. Malic, "Exciton physics and device application of two-dimensional transition metal dichalcogenide semiconductors," npj 2D Materials and Applications **2**, 1–12 (2018).
49. C. Manolatou, M. J. Khan, S. Fan, P. R. Villeneuve, H. A. Haus, and J. D. Joannopoulos, "Coupling of modes analysis of resonant channel add-drop filters," IEEE Journal of Quantum Electronics **35**, 1322–1331 (1999).
50. I. Datta, S. H. Chae, G. R. Bhatt, M. A. Tadayon, B. Li, Y. Yu, C. Park, J. Park, L. Cao, D. N. Basov, J. Hone, and M. Lipson, "Low-loss composite photonic platform based on 2D semiconductor monolayers," arXiv:1906.00459 [physics] (2019).
51. C. T. Phare, Y.-H. D. Lee, J. Cardenas, and M. Lipson, "Graphene electro-optic modulator with 30 GHz bandwidth," Nature Photonics **9**, 511–514 (2015).
52. M. S. Choi, A. Nipane, B. Kim, M. Ziffer, I. Datta, A. Borah, Y. Jung, B. Kim, D. Rhodes, A. Jindal, Z. Lamport, M. Lee, A. Zangiabadi, M. Nair, T. Taniguchi, K. Watanabe, I. Kymissis, A. Pasupathy, M. Lipson, X. Zhu, W. J. Yoo, J. Hone, and J. Teherani, *Achieving High Carrier Density and High Mobility in Graphene Using Monolayer Tungsten Oxyselenide* (In Review, 2021).

LIST OF ACRONYMS, ABBREVIATIONS, AND SYMBOLS

ACRONYM	DESCRIPTION
2D	two dimensional
ALD	atomic layer deposition
CMP	chemical mechanical polishing
CVD	chemical vapor deposition
CW	continuous wave
dB	decible
DC	direct current
DPSK	differential phase-shift keying
DUV	deep ultraviolet
EBL	electron-beam lithography
FEM	finite element model
GHz	gigahertz
HSQ	hydrogen silsequioxane
ICP-RIE	inductively coupled plasma-reactive ion etching
ITO	indium tin oxide
LiDAR	light detection and ranging
LPCVD	low-pressure chemical vapor deposition
MMI	multimode interference
MOCVD	metal-organic chemical vapor dpeposition
MZI	Mach–Zehnder interferometer
NIR	near infrared
ODL	optical delay line
PC	polarization controller
PD	photodiode or photo detector
PECVD	plasma-enhanced chemical vapor deposition
PMMA	poly methyl methacryalate
RC	resistor-capacitor
RI	refractive index
RIE	reactive ion etching
RIU	relative intensity units
rms	root mean square
SiN	silicon nitride
TMD	transition metal dichalcogenide
TLM	transmission line measurement

APPENDIX
EXTRANEOUS DATA

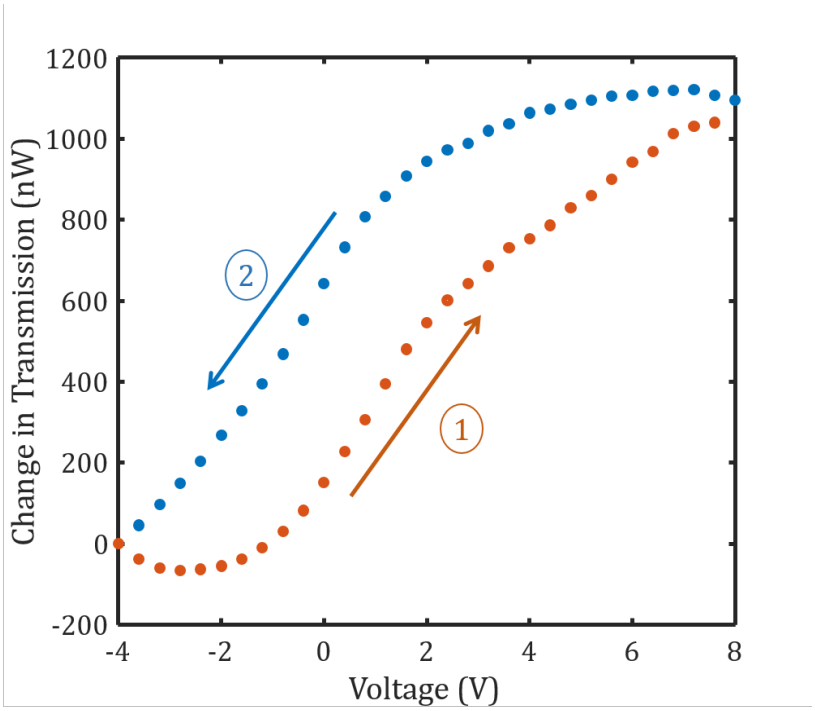

Figure A-1: Hysteresis in SiN-TMD capacitive devices

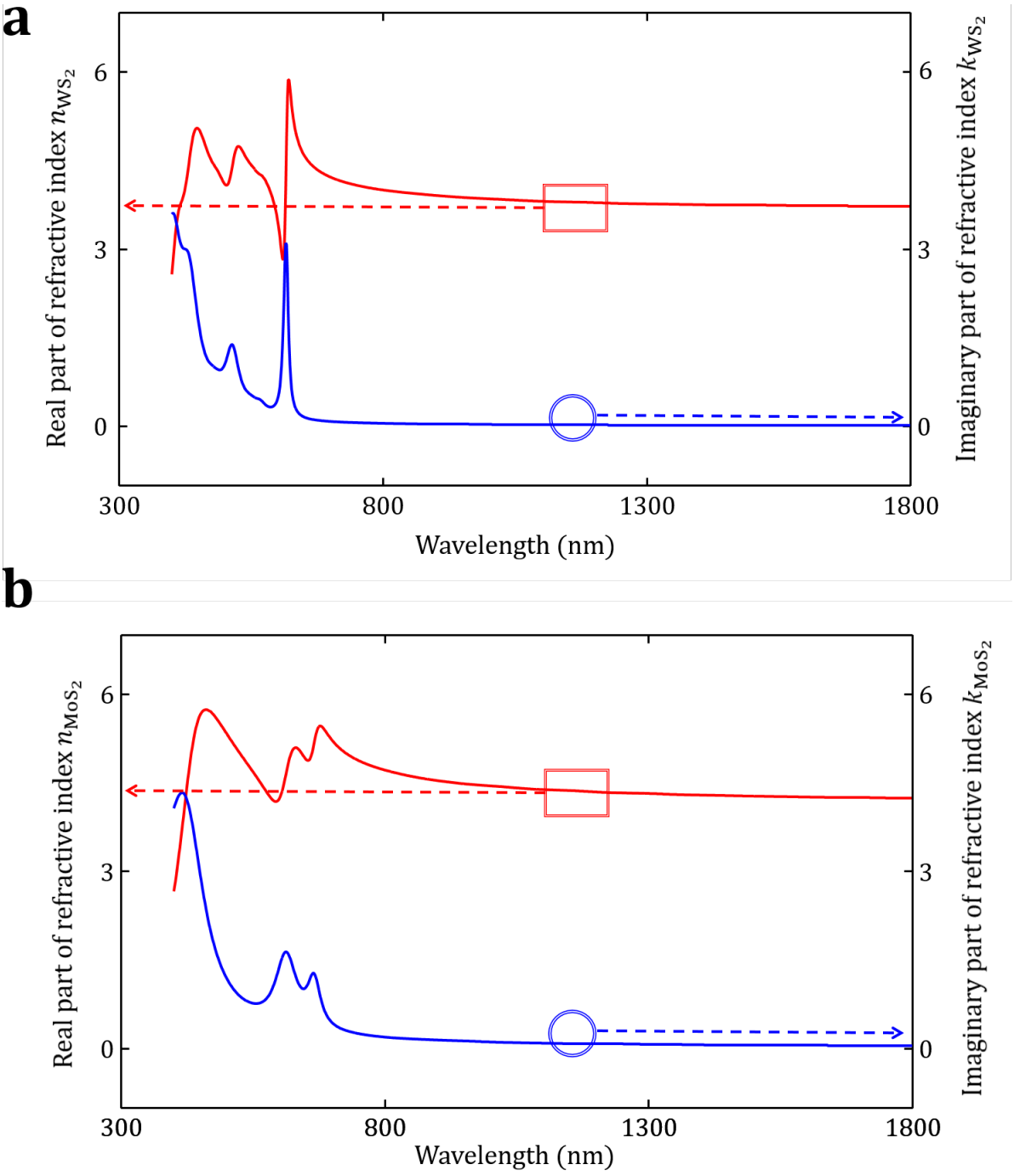

Figure A-2: Real and imaginary part of the refractive index for monolayer TMDs

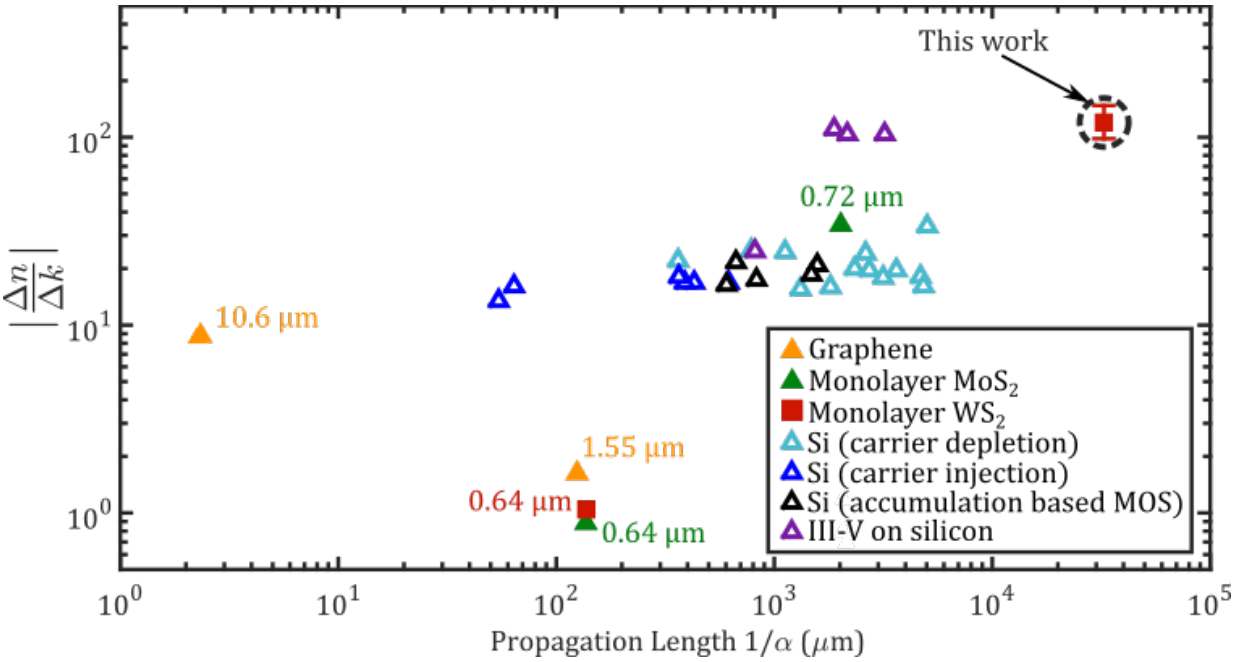

Figure A-3: Detailed comparative analysis of |Δn/Δk| for various monolayer 2D and bulk materials

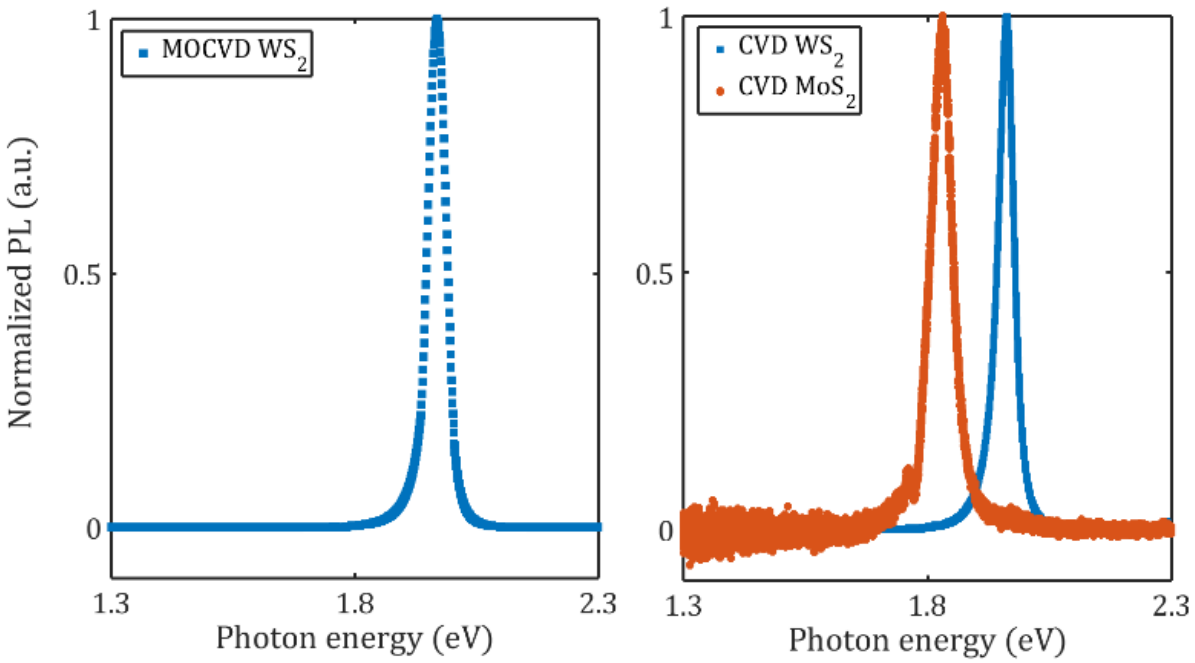

Figure A-4: Normalized PL spectra for monolayer MOCVD WS_2 used in ionic liquid experiments and monolayer CVD WS_2 and MoS_2 used in capacitive photonic structures.

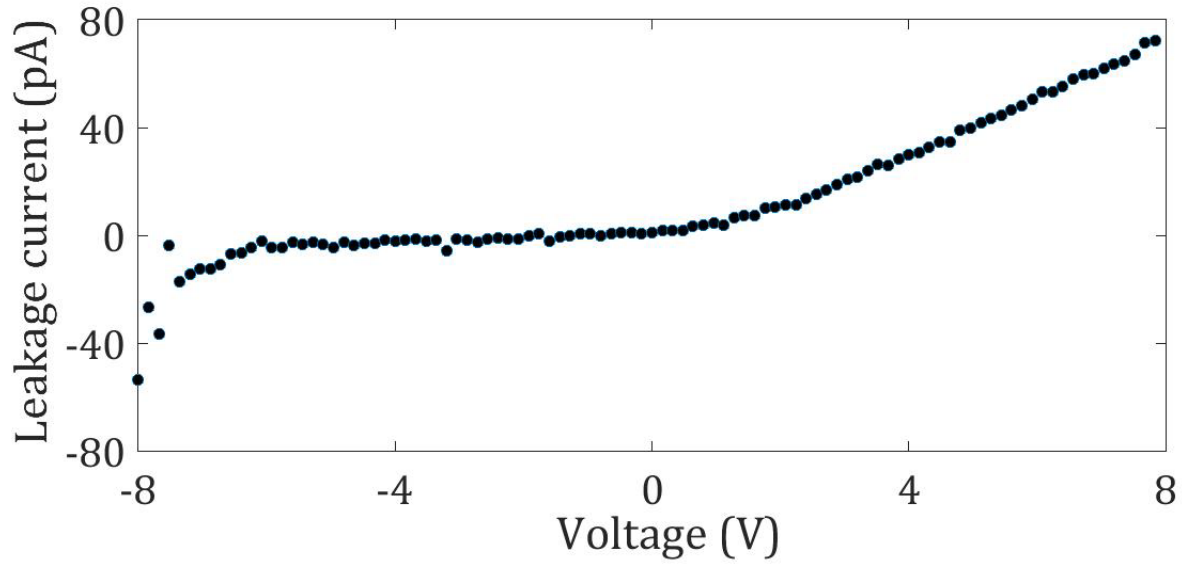

Figure A-5: Leakage current in WS_2-HfO_2-ITO capacitor integrated on a SiN waveguide

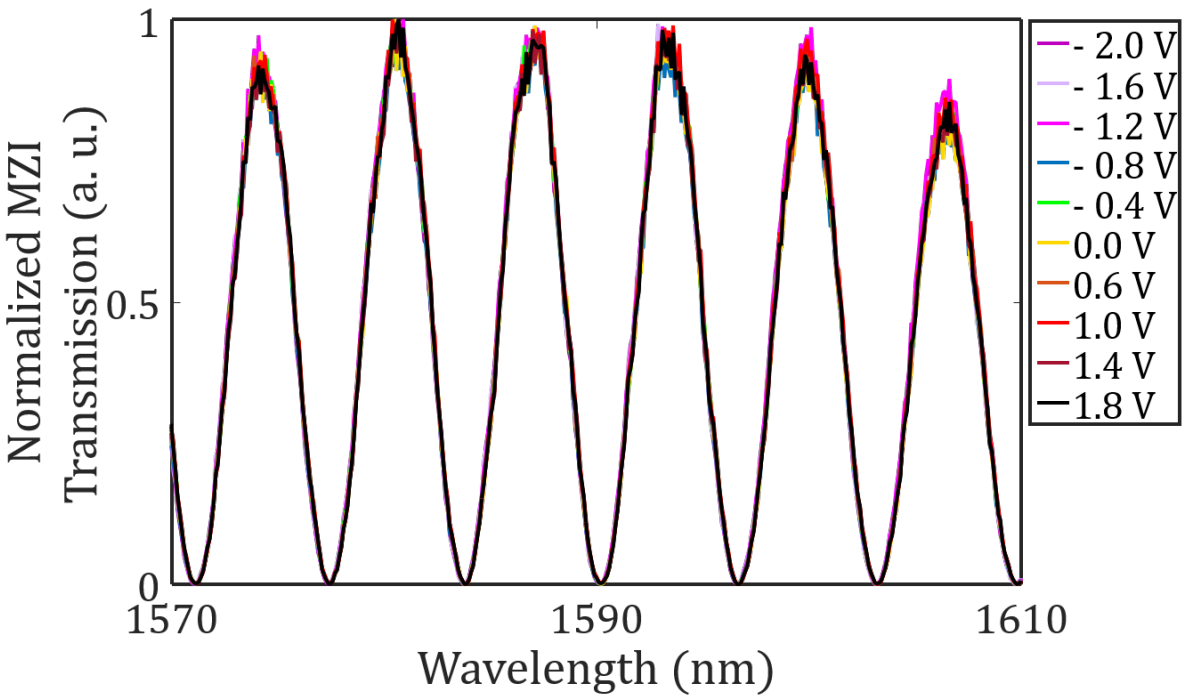

Figure A-6: Normalized MZI Transmission with different voltages applied across the electrodes immersed in ionic liquid, with NO monolayer WS_2 on the SiN waveguides.

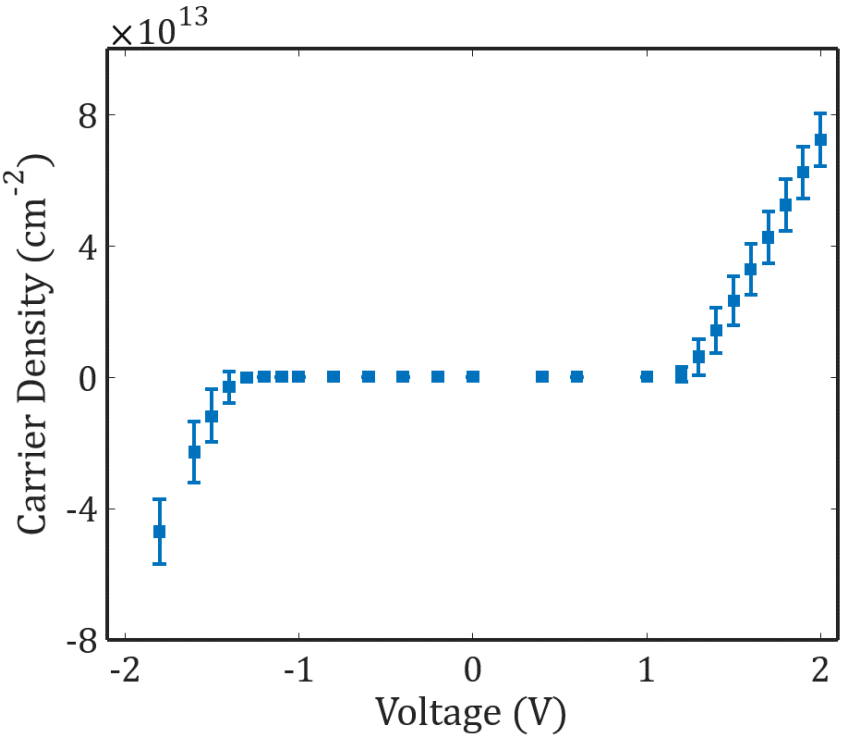

Figure A-7: Theoretically computed carrier doping in monolayer WS_2 with the applied voltage.

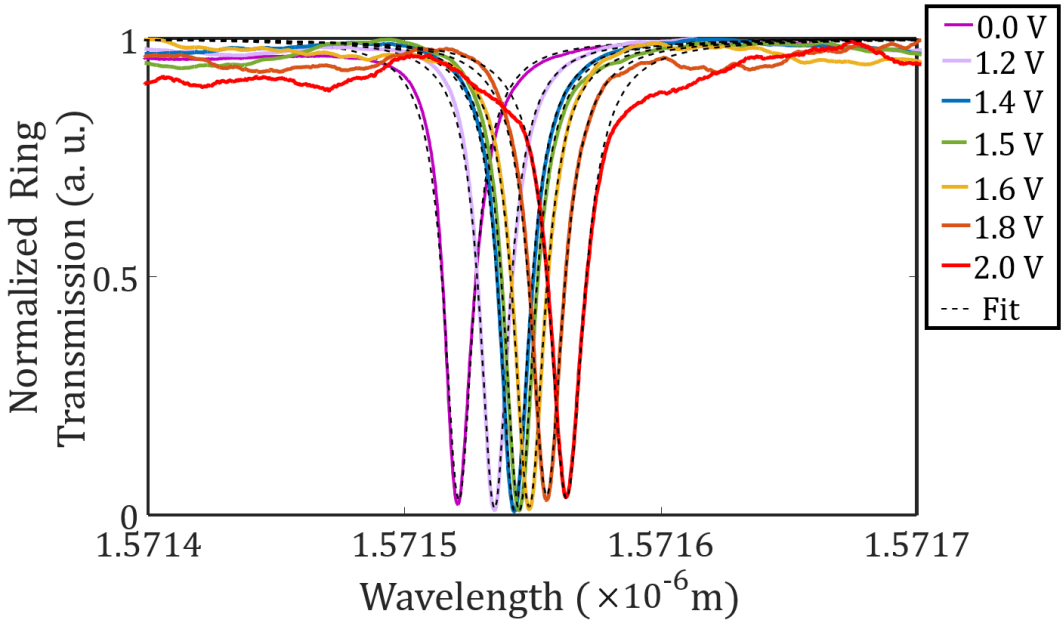

Figure A-8: Calculation of the effective index of the propagating mode with monolayer WS_2 gating through the ionic liquid.